Nano Research

Open Access

Mini Review

Progress of crystalline carbon nitride in synthesis, atomic structure characterization and photocatalysis

Yueyang Tan[1,2,3], Zhongyan Zhang[2], Yayun Pu[5], Zongzhao Sun[4] ✉, and Limin Huang[2] ✉

[1] School of Materials Science and Engineering, Harbin Institute of Technology, Harbin 150001, China
[2] Department of Chemistry, Southern University of Science and Technology, Shenzhen 518055, China
[3] School of Traffic and Environment, Shenzhen Institute of Information Technology, Shenzhen 518172, China
[4] College of Chemistry and Chemical Engineering, Linyi University, Linyi 276000, China
[5] School of Optoelectronic Engineering, Chongqing University of Posts and Telecommunications, Chongqing 400065, China

Cite this article: *Nano Research*, **2025**, *18*, 94907047. https://doi.org/10.26599/NR.2025.94907047

ABSTRACT: Crystalline carbon nitride (CCN) has emerged as a highly promising semiconductor photocatalyst with unique properties, such as enhanced charge migration rate, reduced carrier recombination probability, narrow band gap and improved light-harvesting efficiency, which are suitable for a wide range of applications in solar-to-chemical conversion, energy storage, therapeutic and environmental pollution degradation. In the past few years, there has been an increasing number of reviews on CCN materials. However, most of these reviews mainly focus on synthesis methods, modification and applications, with less emphasis on the relationship between structures and properties, as well as on in-depth exploration of the crystalline structure. The electronic instability of CCN presents challenges for conventional characterization techniques to directly and thoroughly investigate the relationship between its intrinsic atom structure and photocatalytic performance. This mini-review not only highlights the progress in CCN-based photocatalysts, with a focus on molten-salt synthesis (including solid-salt-induced crystallization), but also emphasizes the atomic structure characterization by specifically introducing the differential phase contrast (DPC) scanning transmission electron microscopy (STEM) technique, which is essential for enhancing our understanding of the crystal structure and photocatalytic mechanisms of CCNs. Additionally, the review outlines the photocatalytic performance and puts forward potential challenges on CCN studies. This review will provide a clearer understanding of the relationship in developing precise customization strategies for CCN materials and ultimately explain the regularity and specificity of the enhanced performance in targeted photocatalytic systems.

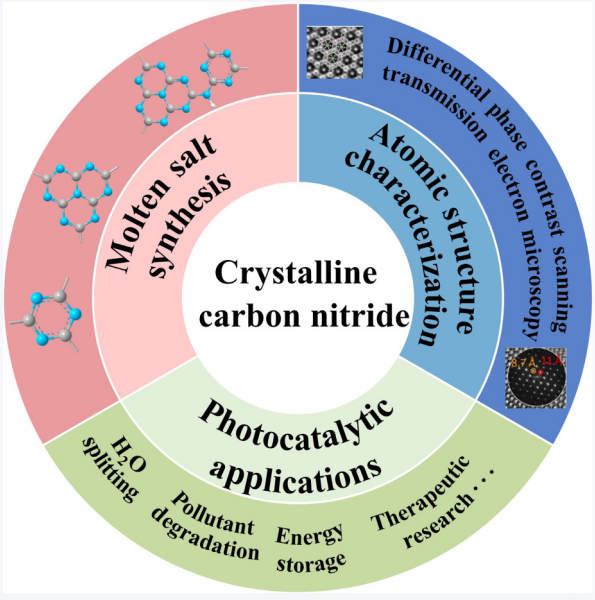

KEYWORDS: crystalline carbon nitride, synthesis, characterization, photocatalysis

1 Introduction

Photocatalytic solar-to-chemical conversion technology stands as a promising strategy to tackle global energy challenges. Numerous semiconductor photocatalysts have been explored to achieve desired performance, including water splitting, CO_2 reduction and the degradation of pollutants [1–4]. In recent years, graphitic carbon nitride (GCN) has emerged as a promising photocatalyst due to the unique properties, such as easy preparation, low cost, nontoxicity, high stability and suitable electronic bandgaps [5–7]. With a suitable bandgap of 2.7 eV, GCN exhibits a desirable visible (vis) light response wavelength less than 475 nm in the solar spectrum. Consequently, GCN has become a popular candidate for

Received: July 16, 2024; **Revised:** September 3, 2024
Accepted: September 23, 2024

✉Address correspondence to Zongzhao Sun, sunzongzhao@lyu.edu.cn; Limin Huang, huanglm@sustech.edu.cn

visible light artificial photocatalysis. However, bulk GCN in the current state is restricted by factors such as poor crystallinity, low surface area, slow charge carrier separation and fast charge carrier recombination [8, 9]. To address these limitations, various strategies have been reported to enhance the photocatalytic activity of GCN, such as improving crystallinity, modifying morphology, doping with elements and constructing heterojunction [10–13].

Improving crystallinity has emerged as a prevalent approach, particularly focusing on crystalline CN (CCN). It is commonly acknowledged that the dynamic hindrance encountered in the traditional solid-phase thermal condensation method frequently results in incomplete condensation and low crystallinity [14]. Studies have demonstrated that promoting the mass mobility of reaction intermediates through the use of molten salts can improve the crystallinity in organic synthesis and electrochemical processes. This revelation has inspired the development of an ionothermal method for synthesizing CCNs by controlling the reaction kinetics.

Often, CCNs prepared through the ionothermal method, using a mixture of monomers and alkaline molten salts, possess a superior photocatalytic activity compared to traditionally thermally synthesized GCNs with amorphous and semi-crystalline structure as high crystallinity and long-periodic structure could effectively enhance charge migration rate, reduce carrier recombination probability, narrow band gap and improve light-harvesting efficiency. The intrinsic properties of CCNs are not only related to the polymeric network, but also determined by the coupled ions in the frameworks. Furthermore, the band gap of CCN could be tuned by altering the stacking arrangement of the conjugated layers. It has also been discovered that alkali metal ions intercalated between the conjugated layers of CCNs facilitate the migration of photogenerated carriers between adjacent layers [15]. Among various CCNs, poly(triazine imides) (PTI) and poly(heptazine imides) (PHI) are considered as ideal models for studying photocatalysis mechanism due to the high crystallinity, well-defined structures as well as the capability for photocatalytic applications. Since Bojdys et al. first introduced the use of a eutectic mixture of LiCl/KCl as the solvent for synthesizing CCN in 2008, there have been many advancements in the photocatalytic applications of CCN [16]. For instance, Domen's group reported a type of PTI synthesized using dicyandiamide (DCDA) and LiCl. The obtained PTI/Li^+Cl^- can function as a photocatalyst producing H_2 or O_2 from water (half reactions) when irradiated with ultraviolet (UV) light (λ > 300 nm) [17]. Wang's group successfully synthesized a heptazine-based CCN through the thermal polymerization of preheated melamine with LiCl/KCl salts. The synthesized material demonstrated significant activity for H_2 production under visible light (> 420 nm) when compared with the reference. They also pointed out the potential for other solar energy applications, including CO_2 reduction, pollutant degradation and organic photosynthesis [18]. The promising photocatalytic applications potential of CCN has spurred more researchers to delve deeper into the photocatalytic applications and properties of CCN.

Noteworthily, the properties of CCNs are closely related to the structures and atomic compositions, making the study of material structures a crucial aspect in the research of CCN [19, 20]. Numerous insightful reviews have already been published on CCNs, covering a range of topics including the catalytic applications and structure design methods [21–25]. For example, Song et al. provide a comprehensive overview of the structural characteristics, photoelectrochemical (PEC) properties, characterization methods, optimization strategies and main applications of CCNs [21]. While the article discusses characterization, it focuses only on conventional techniques such as X-ray diffraction (XRD), solid-state nuclear magnetic resonance (NMR) spectroscopy and high-resolution transmission electron microscopy (HR-TEM), which are insufficient for probing the atomic-scale structure of CCNs. Liu et al. primarily summarize various synthesis methods for CCNs, modification methods to enhance the catalytic performance and diverse applications in photocatalysis [25]. Although the review acknowledges the relationship between the structure and performance of CCNs, it only briefly mentions the importance of HR-TEM in measuring structure, without delving deeper into related techniques and applications for exploring the atomic structure of CCNs. However, elucidating the structures of CCNs down to the atomic scale is rarely achieved due to the instability under high-energy electron beams, which hinders deeper understanding of photocatalysis with these materials. In addition to the topics mentioned in other reviews, this mini-review delves deeply into the advanced electron microscopy technique, specifically differential phase contrast (DPC) scanning TEM (STEM), which plays a significant role in advancing research in the CCN field. Our aim is to provide a comprehensive introduction to the principles of DPC-STEM technology and the application in the structural analysis of CCN. The precise analysis of atomic structure is crucial for gaining a deep understanding of the intrinsic nature of CCNs and uncovering the mechanism that drives the photocatalytic performance. Therefore, the atomic structure analysis of CCNs is currently a topic that deserves significant attention and investigation.

In this mini-review, we summarize the advancements in CCN-based photocatalysts from the perspective of molten-salt synthesis, atomic structure characterization and photocatalytic application, aiming at providing important theoretical guidance that aids the further development of CCN-based photocatalysts. Notably, the DPC-STEM technique for revealing the channel structure of CCNs at atomic-resolution is well discussed to explore the intricate relationships between material properties and structures. This approach enables us to decipher the crystal structure of CCNs, thereby enhancing our understanding of the photocatalytic mechanisms involved in the use of these materials.

2 The research development, synthesis and characterization of CCNs

2.1 The development of CCN

The structure units of CCNs can be categorized into triazine and heptazine subunits. Additionally, the integration of triazine and heptazine units can be obtained by the controlled experimental conditions, as depicted in Fig. 1. Upon comparing the subunit structures, it's evident that each carbon atom in the heptazine subunit is bonded to three nitrogen atoms, forming a relatively stable three-dimensional network. However, in the triazine subunit,

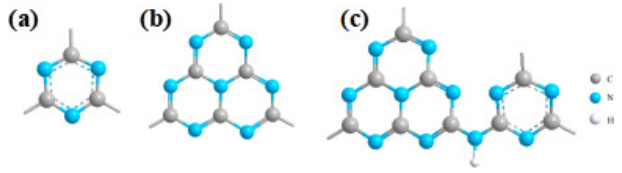

Figure 1 (a) Triazine subunit. (b) Heptazine subunit. (c) The combination of triazine and heptazine units.

each carbon atom is bonded to only two nitrogen atoms, resulting in lower connectivity and weaker bonding compared to the heptazine subunit. The lower stability of the triazine subunit increases the likelihood of structural rearrangements, such as the formation of defects or material decomposition under certain conditions. The heptazine subunit possesses a larger π-conjugated system, resulting in a narrower bandgap, which suggests that heptazine-based CCN can be readily excited, hence enhancing the generation of charge carriers [26]. Furthermore, the differences in grain sizes and crystallinity can affect the physical and chemical properties of the materials. Triazine-based CCN typically exhibits a high specific surface area and strong chemical activity due to the small particle size, making it efficient for catalytic reactions [27]. On the other hand, heptazine-based CCN possesses large grain size and high crystallinity, leading to great electron mobility and optical properties, providing potential applications in optoelectronic devices and other fields [28].

Over the past decade, studies on CCNs for photocatalytic applications, including H_2 production, CO_2 reduction and organics degradation, have significantly increased. The optimization of photocatalytic performance has merged as a key research direction. In this mini-review, we analyzed the Web of Science literature database using the keywords "crystalline carbon nitride/poly(triazine imide)/poly(heptazine imide)" from January 2013 to August 2024. A total of 2555 publications were retrieved. As illustrated in Fig. 2, the publication rate has been steadily increased each year. Notably, the year 2022 witnessed the highest annual publication rate of 366 articles. This trend indicates the rapid progress in CCN research and signifies the emergence of a promising stage of development.

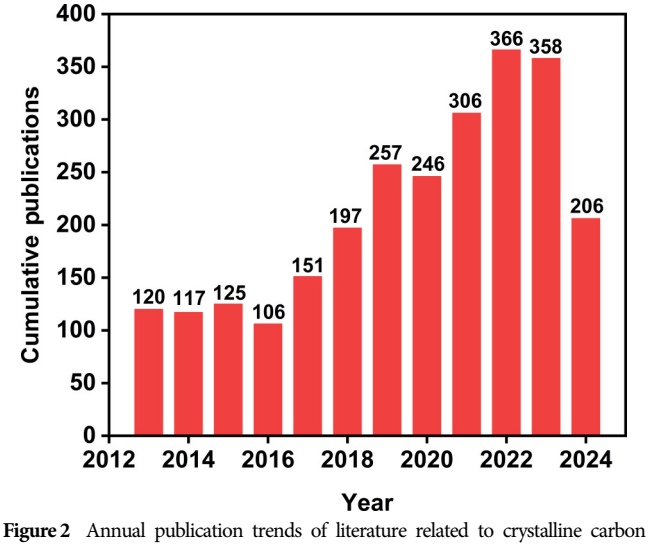

Figure 2 Annual publication trends of literature related to crystalline carbon nitride/poly(triazine imide)/poly(heptazine imide) from January 2013 to August 2024.

2.2 The synthesis of CCN

The synthesis of CCN has a profound impact on the photocatalytic performance of diverse products, encompassing variations in structure, size and morphology. Multiple methods for synthesizing CCN have been put forth, such as high temperature and high pressure (HT-HP) calcination, the template method and the molten salt approach. This review primarily focuses on the molten salt method due to the convenient operation, environmental friendliness and cost-effectiveness. Since then, related research has developed rapidly. The molten salt is known to drive the interunit arrangement by enhancing the intermolecular forces. By selecting suitable molten salts, the crystallinity of products can be further improved by controlling the polymerization process of CCN [29]. Moreover, the intercalation of metal ions into the polymer leads to the formation of robust nitrogen-metal donor–acceptor (D–A) bonds, stabilizing the products and shortening the interlayer distance. This shortened interlayer distance and extended π-system of the products enhance the light-harvesting and charge-carrier transportation properties.

In the molten salt method, a eutectic mixture is used as a solvent due to the high-temperature stability, non-corrosive nature, non-toxicity, excellent solvation of the precursors and a melting point below the polymerization temperature of triazine. These properties facilitate the polymerization of precursors into a carbon nitride network at a relatively low temperature. A selection of commonly used molten salts is presented in Table 1.

Table 1 Properties of some common molten salts

No.	Category	Molten salt	Mass ratio (wt.%)	Melting point (°C)	References
1	Single molten salt	KSCN	—	173	[30]
2	Single molten salt	LiCl	—	605	[17]
3	Single molten salt	NaCl	—	801	[31]
4	Single molten salt	KBr	—	730	[32]
5	Single molten salt	KCl	—	646	[33]
6	Binary molten salt	LiCl/KCl	45:55	352	[34]
7	Binary molten salt	LiBr/KBr	52:48	348	[35]
8	Binary molten salt	LiBr/KCl	75:25	263	[36]
9	Binary molten salt	NaCl/KCl	80:10	650	[37]
10	Binary molten salt	NaCl/LiCl	50:50	552	[38]
11	Binary molten salt	LiCl/$SnCl_2$	20:80	220	[39]
12	Ternary molten salt	NaCl/KCl/LiCl	50:40:10	630	[40]

In general, low-melting-point molten salts are commonly chosen for the synthesis of triazine-based CCN to enhance grain growth and reduce grain size [39–42]. The single molten salts with high melting point, such as NaCl and KCl, listed in Table 1, are typically employed in the synthesis of heptazine-based CCN, as they effectively establish a stable reaction environment conducive to slower grain growth [43, 44]. The unique low-melting-point KSCN plays a key role in enhancing the intermolecular forces of heptazine, which facilitates the polymerization of CCN. As a result, K^+ ions from KSCN can integrate into the polymeric framework, forming a rigid PHI structure [45]. The triazine-heptazine heterostructure has been synthesized through calcining preheated melamine and binary molten salts in the air [20]. However, the selection of molten salt should consider a variety of factors, including specific synthesis conditions and the desired properties of the resulting products.

There are two primary types of synthesis processes for CCN using the molten salt method. One process involves initially forming large pieces of carbon nitride through heat-induced pyrolysis at relatively low temperatures utilizing nitrogen-rich precursors such as melamine, dicyandiamide, urea and others. These large pieces of carbon nitride are subsequently mixed and polymerized with molten salts at high temperatures, resulting in a product containing heptazine ring units. Another synthesis process

involves directly grounding and annealing a mixture of nitrogen-rich precursors and molten salts. The product obtained through this process typically contains triazine units. Take melamine and KCl/LiCl as an example, the resulting products vary depending on the reaction conditions. The possible synthesis processes for different CCNs are shown in Fig. 3.

In the first method, a mixture of melamine and melem can be obtained by preheating melamine within the temperature range of 400 to 550 °C. Subsequently, the precursors obtained in the first step are calcined in a mixture of KCl and LiCl at 550 °C. The triazine-heptazine heterostructures can be synthesized in the air, while heptazine-based CCN can be polymerized from the precursor at 550 °C under inert N_2 conditions. In the second method, triazine-based CCN can be formed by directly calcining melamine in molten salt in the air. Notably, the types of products formed in these reactions are significantly influenced by the gas atmosphere in which they occur. Specifically, the presence of nitrogen atmosphere allows for the further polymerization of the triazine unit into heptazine-based CCN. On the other hand, when the reaction takes place in an air atmosphere, the doping of oxygen into the triazine unit prevents the polymerization into heptazine-based CCN. Consequently, the only product obtained under an air atmosphere is triazine-based CCN, which is produced using melamine as the precursor and molten salts as the liquid reaction media [20].

The synthetic methods for CCN mentioned above both involve the utilization of a mixture of eutectic salts with melting points below the polymerization temperature of the precursors. Several studies have investigated the potential of utilizing a single molten salt for the synthesis of CCN. Some single molten salts with a higher melting point than the precursor polymerization temperature are considered as solid templates, creating an inter-crystal confined space that effectively directs the growth of CCN. Xu et al. successfully synthesized a type of CCN featuring a heptazine framework by employing KCl as a salt template [33]. The researchers initially calcined a mixture of melamine and KCl at 550 °C under an atmospheric environment. Following this process, the CCN was achieved by extensively washing it with distilled water to eliminate the KCl.

2.3 The atomic structure characterization of CCN

The great catalytic efficiency of CCNs is attributed to the condensed polymerization degree and long-periodic structure [46]. The high crystallinity results in faster charge migration, lower intensity of structural defects, reduced recombination probability, narrowed bandgap and enhanced light-harvesting efficiency. Furthermore, the ions in the structure can also impact the catalytic efficiency of CCNs. In the synthesis of CCN with triazine units utilizing DCDA and LiCl/KCl, Li^+ and Cl^- ions are incorporated into the triazine imide network. These ions can modify the electronic properties and energy band structure of the material by either withdrawing or donating electrical charges within the polymer framework. McDermott et al. discovered that the valence and conduction band (CB) edges could be regulated by controlling the loading of Li^+ and Cl^- ions [47]. A decrease in the CB minimum energy occurred due to the splitting of inequivalent unoccupied N states resulting from the interaction with Li^+ ions which replacing H^+ ions in the imide between triazine units. The determination of the valence band (VB) maximum could be attributed to the presence of Cl^- ions, as the Cl 2p electrons, characterized by the low binding energy, occupy the highest energy states in the VB. The adjustment of band structure will further affect the photocatalytic activity of the material. When the catalyst is irradiated with energy equal to or greater than its band energy gap, the electrons on the VB are excited and transit to the CB. This generates positively charged holes in the VB and negatively charged electrons in the CB. These resulting electrons and holes exhibit potent reducing and oxidizing characteristics, which depend on the positions of the conduction and valence bands [48]. Greater reducibility of photogenerated electrons is associated with a more negative CB potential, while stronger hole oxidation is linked to a more positive potential in the VB. Therefore, enhancing the hydrogen evolution capability of PTI/LiCl could be achieved through selectively removing Li^+ ions while maintaining a full Cl^- ions loading. In addition to the ions embedded within the layers, alkali metal ions intercalated between the layers of CCNs can also impact catalytic performance by promoting the migration of photogenerated carriers across adjacent layers [49].

Based on the afore-mentioned reasons, the identification of the

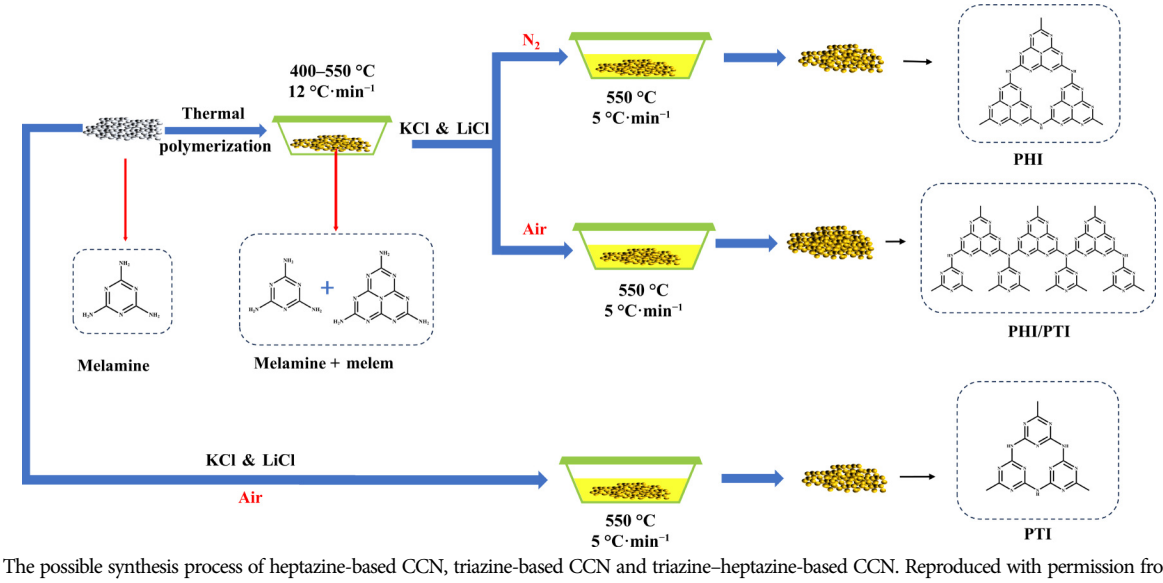

Figure 3 The possible synthesis process of heptazine-based CCN, triazine-based CCN and triazine–heptazine-based CCN. Reproduced with permission from Ref. [20], © Elsevier B.V. 2019.

atomic configuration of CCNs can contribute to exploring the potential physicochemical properties, hence enabling a deeper understanding of the catalytic mechanism.

TEM is the most intuitive method for analyzing the atomic structure of CCNs. However, the unstable nature of CCNs under the high-energy electron beam hinders the elucidation of the structure down to the atomic scale under normal circumstances. Additionally, the commonly used TEMs face challenges in imaging light atoms or suffering from a low signal-to-noise-ratio (SNR). Recently, a new technology, DPC-STEM has emerged. With the merit of a low electron beam dose and high contrast for light elements, it can be used to identify the information about CCNs at the molecular level. By utilizing a four-quadrant detector, integrated DPC (iDPC) STEM can capture the movement data in the *X* and *Y* directions. Furthermore, two-dimensional (2D) integration can produce an image that approximately describes the distribution of the internal potential of the sample projection. The schematic diagram of DPC-STEM is shown in Fig. 4(a) [50]. Nowadays, this technology has achieved direct imaging of light elements, such as oxygen/nitrogen in the field of materials science. Furthermore, it has enabled atomic resolution imaging of electron beam-sensitive metal-organic frameworks at low doses, thereby making successful research on electron beam-sensitive materials possible [51, 52]. Wang et al. studied the beam-sensitive PTI using both iDPC and differentiated DPC (dDPC) STEM techniques [50]. Previously, high-resolution annular dark field (ADF) STEM and HR-TEM had failed to capture the detailed structure of triazine units within PTI crystal. Moreover, the lightest element configuration (Li/H) in the structure, which correlates to the electronic structure for photoabsorption, remained unobservable. In the research, the atomic structure of PTI was revealed by aberration-corrected (AC) DPC-STEM imaging with an ultra-low probe current of 2 pA. Figures 4(b) and 4(e) display the *x* and *y* components of the DPC image, calculated as $DPC_x = A - C$ and $DPC_y = B - D$, where *A*–*D* correspond to the recorded results from the four segments of the detector shown in Fig. 4(a). As presented in Figs. 4(c) and 4(f), a 2D integration of the DPC image provides more details of the PTI [001] lattice. Figures 4(d) and 4(g) present the magnified views of dDPC and iDPC figures. These images were used to clearly resolve the honeycomb structure, the insertion of Cl^- anions and the arrangement of the lightest elements Li and H within the cavities of PTI skeleton. Additionally, direct imaging of the atomic electric field within the PTI crystal revealed the coupling electric field between Li and neighboring triazine units, providing an alternative transfer pathway for photoinduced charge carriers in the corrugated layer. The DPC-STEM imaging technique not only enhances our understanding of the photocatalytic mechanism of PTI crystals but also serves as a valuable tool in the design of efficient photocatalysts.

Wang's group also directly revealed that the prismatic $\{10\bar{1}0\}$ planes are more photocatalytically reactive than the basal {0001} planes in PTI single crystals by using iDPC-STEM [14]. In Figs. 5(a) and 5(c), the high-resolution iDPC image showed the PTI crystals aligned along two orthogonal directions, namely [0001] and $[2\bar{1}\bar{1}0]$. The bright spots in iDPC images directly correspond to atomic columns. The positions of C, N and Cl atoms overlapped and several representative Li^+ ions were highlighted by red arrows in Fig. 5(b). The crystal of PTI/Li^+Cl^- exhibited six prismatic planes aligned edge-on along the *c*-axis, while the side faces were consistently terminated with Cl^- anions. Additionally, dense {0001} conjugated layers were separated by Cl^- anions.

Despite the advantages of DPC-STEM mentioned above, the local structure of PHI at the atomic scale has been infrequently explored due to large spatial distortion and sensitivity to high-energy beams. Even so, Lotsch's group successfully derived the detailed structure of K-PHI and H-PHI using HR-TEM and solid-state NMR spectroscopy, which was further supported by quantum-chemical calculations [53]. Figure 6 showcases a planar, imide-linked heptazine backbone with trigonal symmetry in both K-PHI and H-PHI. The interlayer spacing of H-PHI is measured to be 11 Å in Fig. 6(a). The consistency between the observed (Fig. 6(b)) and simulated (Fig. 6(c)) selected area electron diffraction (SAED) patterns along the [001] zone axis, utilizing the structural model presented in Fig. 6(d), suggests the presence of trigonal layer symmetry in H-PHI. The fast Fourier transform (FFT) result (inset in Fig. 6(a)) verifies the 6-fold symmetry of the diffraction pattern

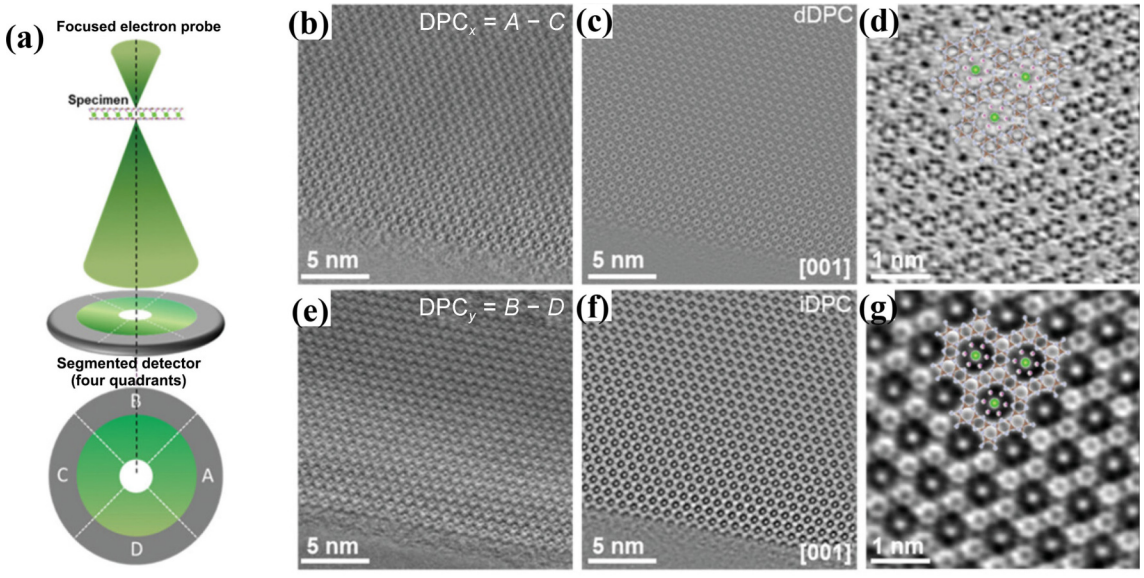

Figure 4 (a) The schematic graph of DPC-STEM. ((b) and (e)) The DPC image calculated as $DPC_x = A - C$ and $DPC_y = B - D$. scale bar, 5 nm. ((c) and (f)) dDPC and iDPC images of PTI along the [001] zone axis. ((d) and (g)) The magnified iDPC-STEM image of PTI. Reproduced with permission from Ref. [50], © Wiley-VCH GmbH 2021.

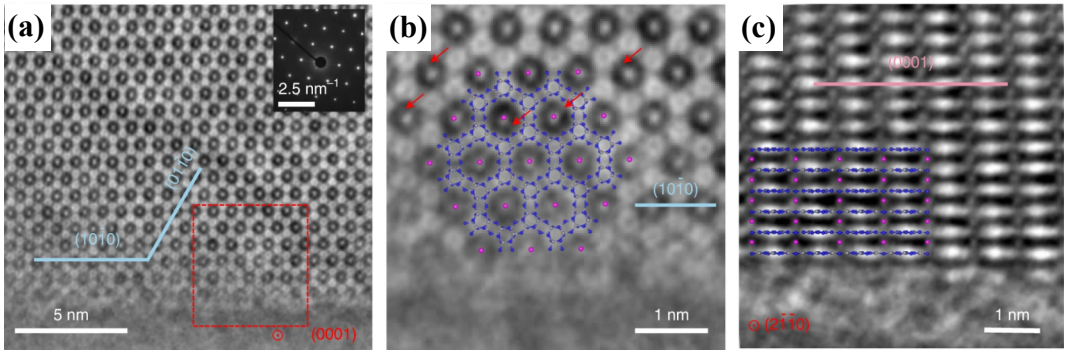

Figure 5 ((a) and (c)) AC-iDPC images of a typical PTI/Li$^+$Cl$^-$ crystal aligned along the [0001] direction and [2$\bar{1}\bar{1}$0] direction, respectively. (b) Expanded view of the red box in (a). Reproduced with permission from Ref. [14], © Lin, L. H. et al. 2020.

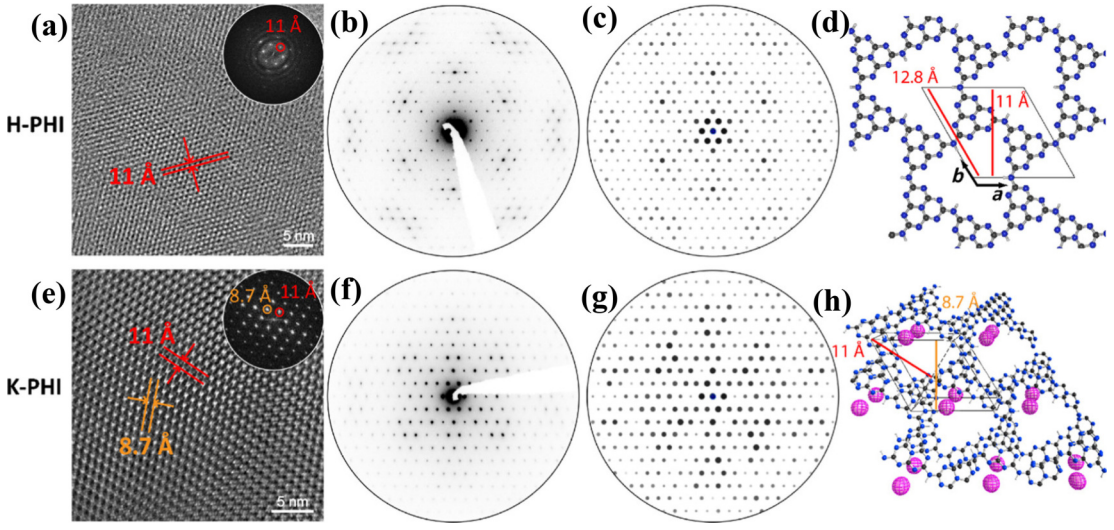

Figure 6 ((a)–(d)) The HR-TEM, SAED pattern, simulated SAED pattern of the [001] zone axis and structural models of H-PHI. ((e)–(h)) The high-resolution TEM, SAED pattern, simulated SAED pattern of the [001] zone axis and structural models of K-PHI. The insets in (a) and (e) display the FFT results for H-PHI and K-PHI, respectively. Reproduced with permission from Ref. [53], © American Chemical Society 2019.

for H-PHI, aligning well with the depicted SAED patterns. The HR-TEM image in Fig. 6(e) reveals distances of 11 Å for the 110 and 8.7 Å for the 100 reflections. The diffraction spots observed in Fig. 6(f) suggest that K-PHI displays monoclinic layer symmetry. Both the simulated SAED pattern (Fig. 6(g)) and the FFT (inset in Fig. 6(e)) yield consistent diffraction results. The difference in symmetry indicates an altered stacking behavior in K-PHI and H-PHI. Further analysis through pair distribution functions highlights the crucial role of the pore content in determining this type of structure. The in-plane structure of K-PHI features a unique layer offset, manipulated by hydrated potassium ions, whereas H-PHI shows a higher prevalence of stacking faults due to the reduced structural guidance from pore water. This study reveals that a decrease in in-plane coherence, reflected in smaller lateral platelet sizes and more terminal cyanamide groups, correlates with enhanced photocatalytic activity.

Currently, many researchers are interested in exploring single-atom catalysts based on CCNs using ion-exchange method. This primarily involves replacing the metal cations in CCN materials with different cations to enhance the catalytic performance of CCNs [54–56]. In majority of studies, researchers mainly utilized the high-angle ADF (HAADF)-STEM technique to investigate the presence of single atoms in materials. While this method allows for the visualization of single atoms, the images produced by this technique only depict individual atoms as bright spots and are inadequate for precisely resolving the framework and positioning of different atoms within CCNs. Meanwhile, imaging light and heavy elements in materials simultaneously pose a challenge for the HAADF-STEM technique. By contrast, the DPC-STEM images can provide direct structural insights with an atomic resolution, allowing us to distinguish light atoms from heavy ones, to analyze the specific structure of CCNs and the specific presence of single atoms in the material [57]. Additionally, given the energy sensitivity of carbon nitride materials, employing the DPC-STEM method can assist the research on single-atom catalysts based on CCN materials.

3 The research advances of CCNs

CCN has attracted considerable attention due to a diverse range of applications across various fields. The distinctive structure and properties of CCN make it an excellent candidate for photocatalysis, enabling efficient light absorption and charge separation, which are crucial for energy conversion processes, including water splitting and CO_2 reduction. Recently, research has expanded into additional areas such as energy storage, pollutant photodegradation and biomedical applications. Overall, investigations into CCN focus not only on enhancing performance but also on broadening applicability across diverse technological and environmental domains. A comparison of the photocatalytic performance of related materials is presented in Table 2.

Table 2 Comparison of different photocatalysts

Photocatalysts type	Photocatalysts	Cocatalysts	Photocatalyst mass (mg)	Reactant solution and sacrificial reagents	Light source	Performance	Apparent quantum yield (%)	References
Triazine-based CCN	PTI-LiNaK	Co (0.5 wt.%) + Pt (1 wt.%) + Cr (0.75 wt.%)	100 mg	Water (100 mL)	300 W Xe lamp (> 300 nm)	H_2: 610 μmol·h^{-1}; O_2: 305 μmol·h^{-1}	25 (365 nm)	[40]
	PTI/Li$^+$Cl$^-$	Co (0.5 wt.%) + Pt (1 wt.%)	120 mg	Water (100 mL)	300 W Xe lamp (> 300 nm)	H_2: 189 μmol·h^{-1}; O_2: 91 μmol·h^{-1}	8 (365 nm)	[14]
	PTI-LiNa	Co (0.5 wt.%) + Pt (1 wt.%)	100 mg	Water (100 mL)	300 W Xe lamp (> 300 nm)	H_2: 273 μmol·h^{-1}; O_2: 135 μmol·h^{-1}	12 (365 nm)	[58]
	PTI nanosheet	Pt (2.2 wt.%)	2 mg	Water (9 mL) + TEOA (1 mL)	300 W Xe lamp (> 420 nm)	H_2: 6.4 μmol·h^{-1}	1 (400 nm)	[59]
	PTI·HCl	—	100 mg	Water (100 mL) + $AgNO_3$ (0.01 M) + La_2O_3 (0.2 g)	300 W Xe lamp	H_2:O_2 = 2:1	0.30 (400 nm)	[60]
	$CoCl_2$(qpy-Ph-COOH)/ PTI-LiCl	—	12 mg	$KHCO_3$ (0.5 M, 10 mL) + Na_2SO_3 (0.2521 g)	Kessil light-emitting diode (LED) lamp (390 nm)	CO: 2149 μmol·g^{-1}·h^{-1}	2.03 (390 nm, 172 mW·cm^{-2})	[61]
	DCDBA5	Pt (3 wt.%)	15 mg	Water (17.1 mL) + TEOA (1.9 mL)	100 W white LED array (≥ 410 nm)	H_2: 11,449 μmol·g^{-1}·h^{-1}	15.6 (405 nm)	[36]
	DCDBA5	—	50 mg	Water (25 mL)	100 W white LED array (≥ 410 nm)	H_2O_2: 66.7 μmol·g^{-1}·h^{-1}	—	[36]
	K-PHI-450	Pt (3 wt.%)	50 mg	Water (225 mL) + TEOA (25 mL)	300 W Xe lamp (420–800 nm)	H_2: 82 μmol·h^{-1}	62 (420 nm)	[62]
	CCN	—	50 mg	Water (90 mL) + methanol (10 mL)	300 W Xe lamp (> 420 nm)	H_2O_2: 210 μmol·h^{-1}	—	[63]
	g-CN-1	Pt (3 wt.%)	50 mg	Water (90 mL) + methanol (10 mL) + K_2HPO_4·3H_2O (2.28 g)	300 W Xe lamp (> 420 nm)	H_2: 770 μmol·h^{-1}	50.7 (405 nm)	[18]
	Mel-PHI	Pt (1.75 wt.%)	14 mg	Water (18 mL) + TEOA (2 mL)	300 W Xe lamp (420–800 nm)	H_2: 5570 μmol·g^{-1}·h^{-1}	17.8 (400 nm)	[64]
Heptazine-based CCN	PHI-Co^{2+}	—	50 mg	Water (100 mL) + $AgNO_3$ (0.01 M) + La_2O_3 (0.2 g)	300 W Xe lamp (≥ 420 nm)	O_2: 31.2 μmol·h^{-1}	—	[65]
	RPCN	Pt (3 wt.%)	20 mg	Water (27 mL) + TEOA (3 mL)	300 W Xe lamp (≥ 420 nm)	H_2: 1.4 mmol·h^{-1}·g^{-1}	21 (420 nm)	[66]
	K-PHI	—	300 mg	Water (100 mL) + $AgNO_3$ (1 g) under argon	50 W white LED array (> 410 nm)	O_2: 4.89 μmol·h^{-1}	—	[67]
	80TpCN	—	50 mg	CO_2 and water vapor	300 W Xe lamp (≥ 420 nm)	CO: 176.9 μmol·g^{-1}·h^{-1}	—	[68]
	CCN	—	100 mg	CO_2 gas with a humidity of 86%	350 W Xe lamp (with an AM1.5 filter)	Hydrocarbons: 12.07 μmol·g^{-1}·h^{-1}	—	[69]
	300gel	—	5 mg	Water (2 mL) + CO_2	300 W Xe lamp (> 400 nm)	CO: 25.7 μmol·g^{-1}·h^{-1}	—	[70]
	CCN	Pt (3 wt.%)	50 mg	Water (90 mL) + methanol (10 mL) + KCl (44 mmol)	300 W Xe lamp (> 420 nm)	H_2: 508 μmol·h^{-1}	55 (420 nm)	[63]
	PHI/PTI:LiCl	—	5 mg	Water (2 mL) + methanol (20 vol.%)	White LED system (0.1 W·cm^{-2}, ≥ 400 nm)	H_2O_2: 4 mmol·g^{-1}·h^{-1}	—	[71]
Triazine–heptazine-based CCN	HTCN-500	Pt (3 wt.%)	20 mg	Water (72 mL) + TEOA (8 mL)	350 W Xe lamp	H_2: 890 μmol·h^{-1}·g^{-1}	26.7 (420 nm)	[20]
	CN-NaK	Pt (3 wt.%)	50 mg	Water (38 mL) + TEOA (10 vol.%)	50 W LED light (> 420 nm)	H_2: 278 μmol·h^{-1}	32 (420 nm)	[29]
	SF-CN_{1-3}	Pt (3 wt.%)	20 mg	Water (60 mL) + TEOA (20 mL)	300 W Xe lamp (> 420 nm)	H_2: 18.13 mmol·h^{-1}·g^{-1}	33.2 (420 nm)	[72]
	MA-rod array	Pt (3 wt.%)	20 mg	Water (40 mL) + TEOA (10 mL)	300 W Xe lamp (> 420 nm)	H_2: 11,720 μmol·h^{-1}·g_{cat}^{-1}	60 (420 nm)	[73]
	PHI/PTI	Pt (3 wt.%)	50 mg	Water (90 mL) + TEOA (10 mL)	300 W Xe lamp (> 420 nm)	H_2: 348.5 μmol·h^{-1}	42 (420 nm)	[74]

3.1 Triazine-based CCN

Triazine-based CCNs are typically synthesized through ionothermal methods in a eutectic salt melt, such as LiCl/KCl. In this process, the salts act not only as a good solvent towards nitrides, carbides, cyanides, cyanates and thiocyanates, but also serve as a structural directing agent [57, 75]. As the typical triazine-based CCN, the individual layers of PTI are formed via imide-bridging of triazine rings, resulting in a porous topology characterized by a high density of two-dimensional pores. The resulting PTI layers are organized in an AB stacking, with uniform pores channels aligned along the *c*-axis. Since triazine units are less stable than heptazine units from a thermodynamic perspective, as indicated by the density functional theory (DFT) calculations, the resulting triazine-based structure requires support and stabilization from the eutectic mixture with some ions inserted into the crystal texture. The channels of the synthesized PTI, as indicated by related research, have been found to be embedded with lithium and halide ions, resulting in these compounds being typically referred to as PTI/Li^+Cl^- [76].

As shown in Fig. 7(a), the synthesized PTI/Li^+Cl^- can be viewed as a hexagonal prism, with two hexagonal (0001) facets forming the bottom surface and the sides being made up of six rectangular $(10\bar{1}0)$ facets [77]. In Fig. 7(b), each PTI/Li^+Cl^- has a 2D layered structure in which C atoms and N atoms are connected through sp^2-hybridization. It is found in Fig. 7(c) that Li^+ and Cl^- ions are incorporated along the crystallographic *c*-axis. The Li^+ ions are randomly distributed close to the Cl^- ions to maintain charge balance. The additional bonding between Li^+ ions and subunits within the structure helps to reduce the interlayer distances. As a result, the reduced stacking distance between layers can speed up the charge transfer within the interlamination, which is beneficial to improving photocatalytic performance. Bojdys et al. measured the interlayer distance of PTI using different salt combinations [35]. They found that the interlayer distance was 3.52 Å with KBr/LiBr, 3.38 Å with KCl/LiCl and it decreased to 3.32 Å with KF/LiF.

The mechanism of molten salt assisted crystallization process was deeply explored. Tian et al. pointed out that the molten salt can serve as an *in-situ* template during the nucleation and precipitation process [42]. Liang et al. further delved into the mechanisms underlying the conjugation, nucleation and crystallization processes of PTI [78]. As depicted in Fig. 8, they prepared three products at different polycondensation stages: one retained the crystallization interface between PTI crystal and molten salts (PTI-salt), one consisted of the pure PTI phase (PTI) and one maintained the conjugated molecular structure at high-temperature stages (PTI-Q, where Q refers to the quench step, in which the high-temperature melt was rapidly cooled by immersion in deionized water within less than 1 s). Solid-state ^{13}C cross polarization magic-angle-spinning (CP-MAS) NMR results indicated that PTI-Q already had a LiCl-interacted triazine motif, suggesting that both the depolymerization of heptazine units and the intercalation of salt ions into the triazine interlayers procedures occurred during the heating process. HR-TEM images showed that KCl played a role as a template in the precipitation of PTI crystals, while no fixed orientation relationships were observed between LiCl and PTI crystals. The agglomeration of PTI crystals caused a reduction in the exposed areas of $\{10\bar{1}0\}$ planes.

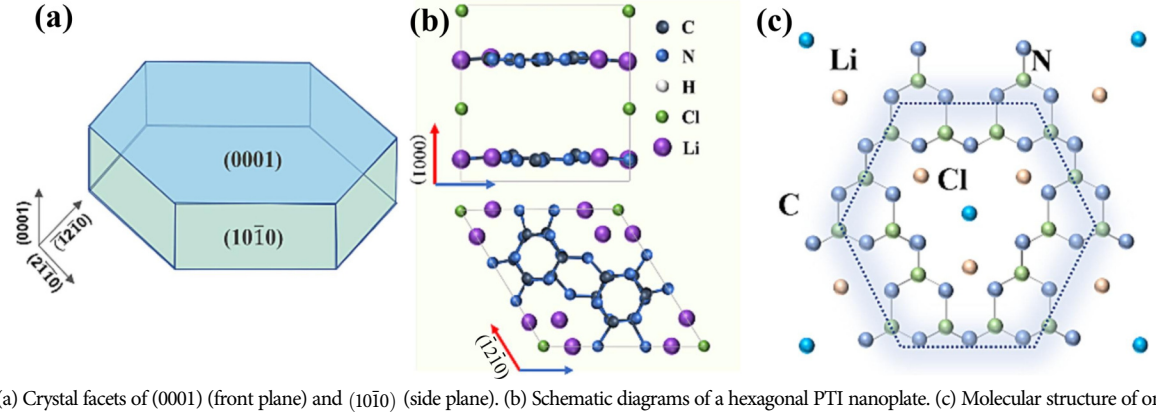

Figure 7 (a) Crystal facets of (0001) (front plane) and $(10\bar{1}0)$ (side plane). (b) Schematic diagrams of a hexagonal PTI nanoplate. (c) Molecular structure of one basic unit of PTI. Reproduced with permission from Ref. [77], © Elsevier B.V. 2023.

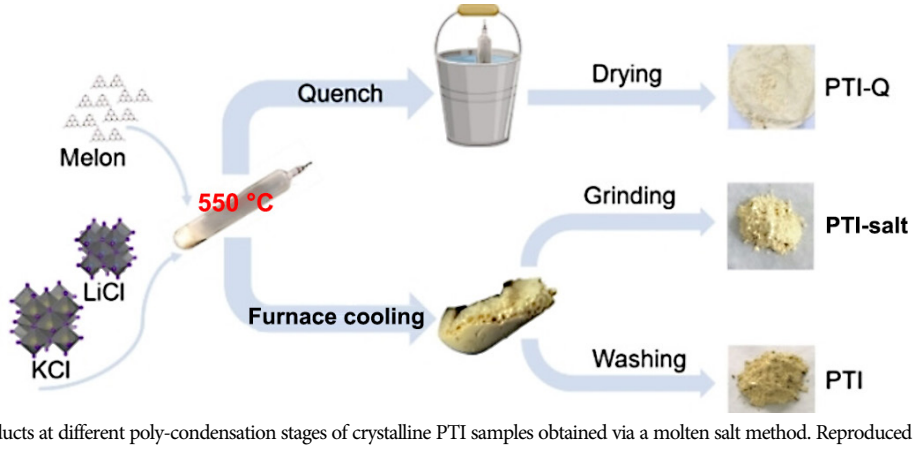

Figure 8 Conjugated products at different poly-condensation stages of crystalline PTI samples obtained via a molten salt method. Reproduced with permission from Ref. [78], © Wiley-VCH GmbH 2023.

McDermott et al. demonstrated that the photocatalytic activity of PTI could be improved by controlling the amount of LiCl loading [47]. X-ray absorption near-edge spectroscopy (XANES) measurements revealed that the bandgap of PTI decreased from 2.8 eV in the absence of LiCl to 2.2 eV for PTI with full LiCl loading. This suggested that the bandgap could be directly tuned by adjusting the quantity of LiCl. Additionally, the morphology of PTI could be modified by changing the amount of molten salt used. Yan et al. reported that precise control of the mass ratio of melamine and molten salt mixture could lead to the formation of layered structures, hollow tubes, or nanosheets [27]. Among these, PTI nanosheets exhibited the highest visible light catalytic activity for the degradation of rhodamine B (RhB) due to the higher bandgap value, specific surface area and efficient separation of photo-generated electron–hole.

The formation of the built-in electric field (BIEF) between Li within the framework cavities of PTI/Li^+Cl^- and the surrounding N not only extends the π-conjugated systems, but also constitutes an additional delivery path of charge carriers between adjacent triazine units, which could facilitate the migration of photogenerated electrons within the corrugated layers of PTI [50]. The photoactivity of PTI, which benefits from the electric field distribution, gives it significant potential in hydrogen production, pollutant degradation, desulfurization and overall water splitting.

The characteristics of PTI crystal structure provide inspiration for designing highly efficient photocatalysts. Wang's group studied the structural characteristics of PTI and further optimized the method, utilizing these characteristics to boost the overall water splitting performance [14]. As mentioned earlier, they discovered that the $\{10\bar{1}0\}$ planes of PTI/Li^+Cl^- was the primary reactive facet for both reduction and oxidation, attracting the deposition of Pt and Co co-catalyst particles. Hence, a method that enlarges the prismatic surface is advantageous for enhancing photocatalytic activity. In the study, the product generated at a synthetic temperature of 550 °C featured a rod-like shape and displayed the best photocatalytic overall water splitting performance compared to the products synthesized at 500 and 600 °C. This superiority can be attributed to the larger surface area. Moreover, triazine units undergo depolymerization at temperatures exceeding 550 °C, leading to structural defects that diminish the photocatalytic activity by serving as charge recombination centers. Inspired by this, the same group also developed a fully condensed PTI photocatalyst with an extended π-conjugated system and a low density of nitrogen defects through ionothermal synthesis from LiCl/NaCl [58]. The catalyst synthesized in LiCl/NaCl with a melting point of 552 °C, which is close to the polymerization temperature, displayed the optimal overall water-splitting performance. The LiCl/NaCl salt melt could create a mild environment for crystal growth and inhibit the depolymerization of triazine units. Enhanced π-conjugation and minimized defects facilitated charge separation, thereby improving photocatalytic efficiency. The PTI-LiNa demonstrated superior overall water splitting performance with stoichiometric H_2 and O_2 generation rates of 273 and 135 μmol·h^{-1}, respectively. Comparative experiments were conducted using molten salts with different melting points to synthesize various PTIs. However, none achieved the exceptional photocatalytic performance for overall water splitting. This is primarily because when the melting point of the molten salt is lower than the condensation points of *s*-heptazine and its derivatives, the incomplete melting and solvation of cyanide-based precursors and intermediates, resulting in incomplete polymerization. Consequently, structural defects hinder the charge carriers separation and migration within the bulk material and at the interface between the photocatalysts and cocatalysts, ultimately impacting photocatalytic performance. If the temperature reaches 600 °C, the issues present at lower temperatures will be resolved. However, the depolymerization of triazine rings will result in undesired structural defects, ultimately reducing photocatalytic activity. The above studies have demonstrated that both surface area and crystallinity can influence the final photocatalytic performance.

Their group's finding also indicated that the photo-induced carriers in PTI tend to migrate in-plane rather than hopping between layers. Therefore, PTI/Li^+Cl^- nanosheets with reduced stacking of triazine-based layers are highly sought after to improve charge migration efficiency. A novel bottom-up synthesis method with LiCl/NaCl/KCl molten salt was developed by their group for designing the crystal growth orientation of 2D polymers (PTI-LiNaK) [40]. The photocatalytic performance of the products synthesized with this ternary salt, containing approximately 10 wt.% Li, was superior. The higher melting point of this molten salt facilitated in-plane conjugation rather than growth along the *c*-axis. A sufficiently lower contents of LiCl enabled the polymerization of PTI/Li^+Cl^- crystals, while NaCl/KCl acted as templates for in-plane polymerization and crystal growth. In contrast to the conventional PTI/Li^+Cl^- single crystal hexagonal prisms synthesized with LiCl/KCl, which yield an apparent quantum yield (AQY) of only 8% for photocatalytic overall water splitting at 365 nm, the optimized PTI-LiNaK nanosheets exhibited a remarkable AQY of 25% at the same wavelength, accompanied by a solar-to-hydrogen conversion efficiency of 0.33%. The evaluation of temperature-dependent photoluminescence (PL) spectra reveals that PTI-LiNaK exhibits the lowest exciton binding energy compared to PTI/Li^+Cl^- references. This observation indicates an extended in-plane π-conjugated structure that facilitates rapid dissociation of singlet excitons into hot charges. Furthermore, steady-state and transient surface photovoltage spectroscopy demonstrate that PTI-LiNaK possesses a higher photovoltage intensity than the references, indicating increased charge migration from the interior to the surface in PTI-LiNaK nanosheets compared to the PTI/Li^+Cl^- prisms. Femtosecond transient absorption spectroscopy comparisons also highlight a prolonged active charge recombination process with a longer lifetime in PTI-LiNaK. These discoveries demonstrate that the significant enhancement in performance is attributed to the efficient separation and transport of photogenerated carriers within the material, facilitated by the extended in-plane π-conjugated.

Lyu et al. obtained Li^+ incorporated highly crystalline PTI (PTI-Li^+) by calcining dicyandiamide in a sealed ampoule with LiCl and KCl molten salt to detect catalytic performance in the selective catalytic oxidation of H_2S [79]. In a continuous reaction process with weight hourly space velocity of 6000 mL·g^{-1}·h^{-1}, PTI-Li^+ achieved a H_2S conversion rate of 98.5%, with a selectivity of 97.4% towards element sulfur. PTI-Li^+ also demonstrates excellent stability during five regeneration tests. This research not only broadens the photocatalytic application of PTI-Li^+ but also deepens the understanding of the relationship between the chemical structure and catalytic performance by exploring the role of atomically dispersed Li ions in PTI-Li^+ during catalytic reaction. A comparison between PTI-Li^+, melon-based polymeric CN and intercalant-free poly(triazine imide) (PTI-IF; a reference with similar chemical and crystal structures was synthesized by employing the Soxhlet extraction method to remove the incorporated ions from PTI-Li^+)

revealed that both the triazine-based structure and Li^+ ions lead to a substantial enhancement in the intrinsic catalytic performance of the catalyst. With the iDPC technique, the arrangement of Li^+ ions within the framework cavities of the PTI-Li^+ crystal was elucidated. DFT calculations revealed the adsorption behavior of O_2 and H_2S on PTI-Li^+. Among the analyzed models, the adsorption energy of O_2 on the Li-terminated PTI-Li^+ (0001) surface (A-Li) was the lowest at −0.99 eV, indicating a strong interaction. Furthermore, the A-Li model exhibited shorter Li_a–O bond lengths of 2.09 and 2.21 Å compared to the other models, underscoring a superior affinity for O_2. Additionally, the O–O bond length was stretched to 1.29 Å (compared to 1.23 Å for gaseous O_2), suggesting that the adsorption and activation of the O_2 are favorable on the A-Li surface. Bader charge analysis and charge density difference calculations revealed that Li^+ exhibited no significant change after adsorbing O_2, the electrons primarily originated from the triazine ring of A-Li. The adsorption behavior of H_2S on A-Li is similar to that of O_2. The analysis suggested that dispersed Li^+ ions in PTI-Li^+ not only serve as active sites for the selective oxidation of H_2S but also function as bridges for electron transfer between the catalyst and reactants. Furthermore, the triazine-based structure and the interaction with Li^+ ions result in an extended electron delocalization and a suitable electron band structure. These factors enhance the adsorption and activation of O_2 and H_2S, ultimately leading to improved catalytic activity and durability in the selective oxidation of H_2S.

Simple adjustment in the size of PTI material can also result in alteration in the performance. Schwinghammer et al. developed a facile aqueous exfoliation method to obtain high crystalline ultrathin PTI nanosheets with excellent photocatalytic water-splitting activity [59]. In Fig. 9, the bulk PTI was sonicated for 15 h in water and centrifuged three times at different rotation speeds. Atomic force microscopy (AFM) results revealed that the exfoliated nanosheets were composed of a few layers, with lateral sizes less than 100 nm and a height of 1–2 nm. The NMR spectrum suggested that the nanosheets after exfoliation were formed of 2–4 layers interspersed with two water layers. HR-TEM and XRD further confirmed that the structure of the bulk PTI was retained in the nanosheets. Due to the higher exposure of active sites and specific surface area, the photocatalytic hydrogen evolution activity of PTI nanosheets was 17 times that of raw melon and 8 times that of bulk GCN [80]. A long-term hydrogen evolving measurement lasting 130 h proved the high stability of these exfoliated nanosheets.

3.2 Heptazine-based CCN

Demonstrated through experimental and theoretical studies, heptazine-based CCN exhibits superior thermal stability. The larger π conjugated system contributes to light harvesting and carrier mobility. The typical PHI is mostly formed by the connection of multiple heptazine units with K^+ ions inserted within the pores, as shown in Fig. 10(a) [81]. The layer-to-layer distance can be determined at 0.34 nm in Fig. 10(b) [16]. PHI stands out as a material with an exceptionally high positive VB potential, which greatly enhances the reactivity of photoexcited holes as strong oxidizing agents. Meanwhile, the negative surface charge of the PHI backbone strengthens the dispersion stability of the photocatalyst through interparticle repulsion, thereby increasing the light exposure surface area of the catalyst and improving the accessibility of reactants in the photocatalytic process. Moreover, the photocatalytic effectiveness of PHI materials is closely associated with the crystal structure [36]. PHI materials that are rich in well-ordered (100) planes exhibit superior photocatalytic performance, owing to enhanced in-plane electron mobility. In addition to the aforementioned features, the modified PHI also possesses near-

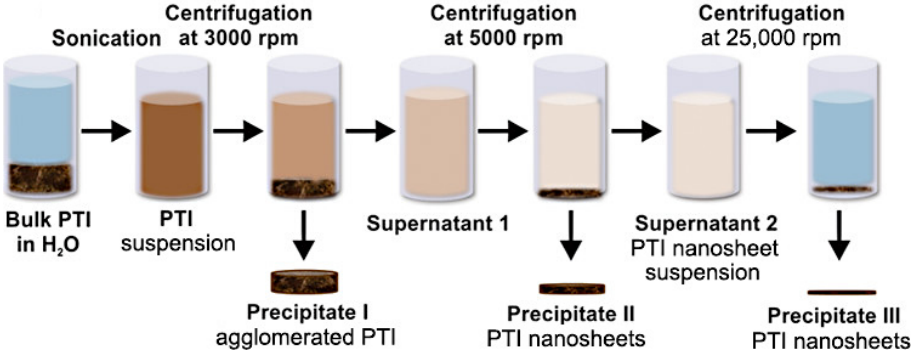

Figure 9 Exfoliation process and product labeling. Reproduced with permission from Ref. [59], © American Chemical Society 2014.

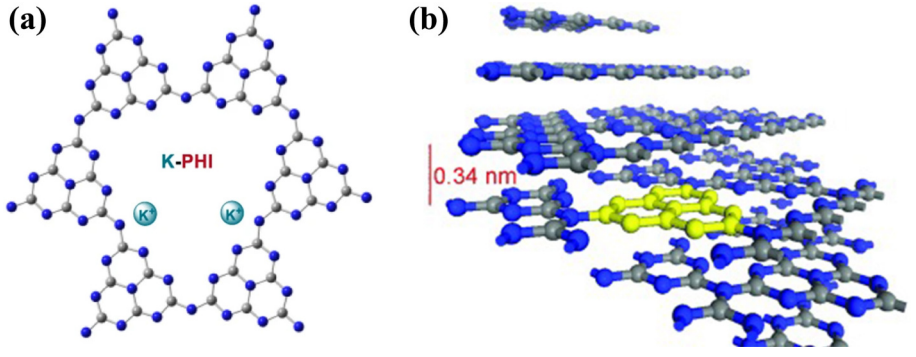

Figure 10 The crystal structure of K-PHI. (a) Reproduced with permission from Ref. [81], © Xing, L. Z. et al. 2023. (b) Reproduced with permission from Ref. [16], © WILEY-VCH Verlag GmbH & Co. KGaA, Weinheim 2008.

infrared (NIR) light photoactivity, energy storage capabilities and other unique characteristics [38, 82, 83]. Consequently, researchers have shown considerable interest in synthesizing and optimizing PHI to achieve a diverse range of applications, such as photocatalytic water splitting, photoelectrochemical water splitting, dark photocatalysis, therapeutic and environment-related applications [23, 45, 84, 85].

Nimbalkar et al. discovered that the photocatalytic efficiency of products derived from different allotropes of GCN varied significantly (Fig. 11) [62]. The melamine was first heated at 450, 550 and 650 °C to achieve different GCN allotropes, specifically melem unit, planar and fractured melon. These were mixed with KSCN for synthesizing high-activity potassium inserted PHI (K-PHI). The product derived from melem units, known as K-PHI-450, exhibited the highest photocatalytic hydrogen production efficiency among the tested samples. The hydrogen evolution rate of K-PHI-450 (84 μmol·h^{-1}) was higher than those of K-PHI-550 and K-PHI-650 by 1.3 and 1.9 times, respectively. The AQY of K-PHI-450 for hydrogen evolution reached 62% at 420 nm, surpassing most reported heptazine-based CCN. K-PHI-Ts exhibited UV–vis spectroscopy absorption edges around 460 nm, indicative of the π→π* transition of the conjugated aromatic system. The absorption tail beyond 460 nm, related to the excitation of electrons to defect states, displayed an intensity ranking of K-PHI-650 > K-PHI-550 > K-PHI-450. This trend suggests that K-PHI materials synthesized from less condensed precursors, such as melem units, possess a more intact structure with fewer defect states. A more intact structure enhances the separation of photogenerated charges, thereby improving photocatalytic activity. In the FTIR spectra of K-PHI-Ts, a peak at 2180 cm^{-1}, assigned to peripheral cyanamide functional groups, was observed. Notably, K-PHI-450 displayed the highest intensity at this peak due to the greater number of peripheral cyanamide groups resulting from a larger surface area. Further, time-resolved PL (TRPL) measurements on aqueous suspension of K-PHI-Ts with an electron donor revealed that K-PHI-450 possessed a shorter emission lifetime compared to K-PHI-550 and K-PHI-650. This observation suggests that the trapped electrons in the long-lived states of K-PHI-450 are more likely to interact with species in the solution before undergoing radiative recombination, a phenomenon facilitated by the higher content of cyanamide functional groups. The combination of intact structure and high cyanamide content facilitates charge transfer and separation, ultimately contributing to the superior photocatalytic performance of K-PHI-450. Moreover, K-PHI-450 could be used to reform cellulose for producing hydrogen and biochemical under visible light irradiation. These results collectively demonstrated that the structural intactness and the functional group of K-PHIs could be tuned by optimizing the precursors and finally affect the photocatalytic performance.

Lotsch's group and co-workers developed a covalent surface modification method for 2D PHI by mixing K-PHI with ammonium chloride and dicyandiamide (Fig. 12) [64]. Ammonium chloride was used to enhance the reversibility of the polycondensation reaction by adjusting the autogenous ammonia pressure during synthesis. The terminal cyanamide of K-PHI reacted with the molten dicyandiamide to form melamine and ultimately generated a surface functionalized Mel-PHI. The same in-plane reflexes of K-PHI and Mel-PHI in XRD spectra in Fig. 12 suggested that the polymer backbone remained unchanged. The FTIR, {^{1}H}^{13}C CP NMR, an in-depth MAS solid-state NMR spectroscopy analysis all confirmed the existence of melamine moiety in Mel-PHI. The effects of melamine functionalization on charge carrier separation and extraction at the PHI surface were thoroughly investigated. As depicted in Fig. 12(a), while both Mel-PHI and K-PHI have a band gap of 2.7 eV, ultraviolet photoelectron spectroscopy reveals that the VB edge of Mel-PHI is positioned 0.4 eV closer to the vacuum level than that of K-PHI. The shift provides a greater driving force for photoexcited electrons in the conduction band of Mel-PHI. To further investigate charge

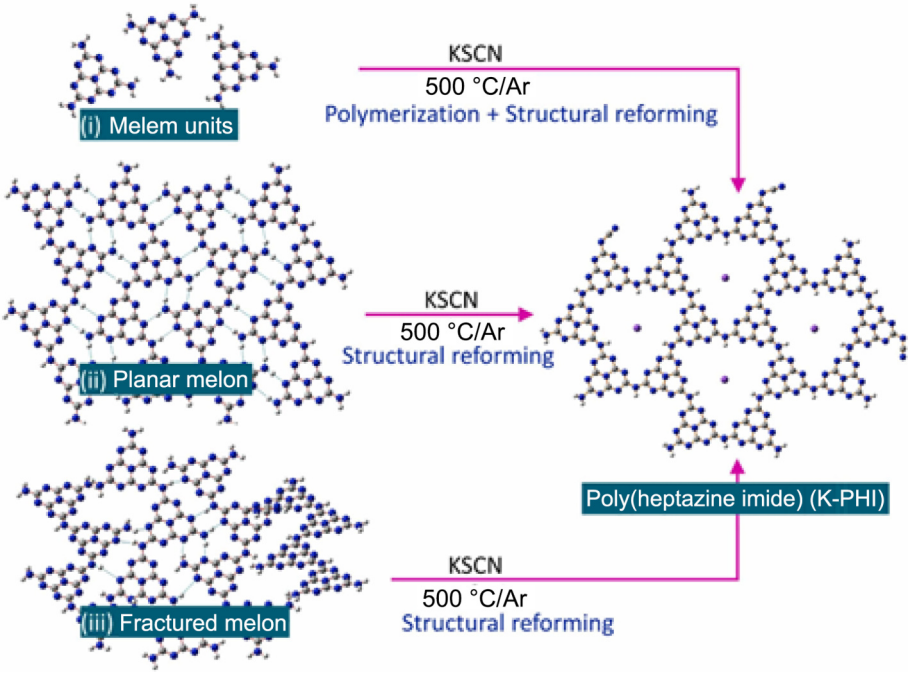

Figure 11 Preparation of K-PHI photocatalysts using different GCN allotropes (blue: N, gray: C; white: H; purple: K). Reproduced with permission from Ref. [62], © Elsevier B.V. 2022.

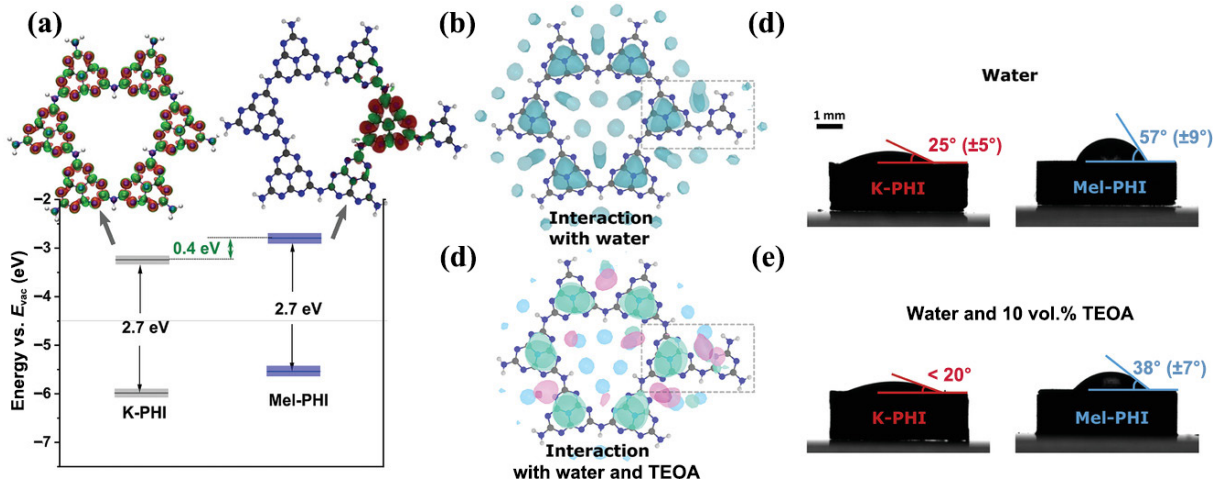

Figure 12 Band position analysis and quantum-chemical evaluations of spin density delocalization and interaction with water and TEOA. (a) The band gap and difference densities of exciton delocalization after excitation of Mel-PHI and K-PHI. (b) Interaction of the Mel-PHI model with water. (c) Interaction of the Mel-PHI model with TEOA and water. Blue areas represent the interaction with water, green areas highlight the N atoms of TEOA and red areas show the OH groups. Contact angle measurement images of (d) water wetting and (e) water wetting with 10 vol.% TEOA after 30 s of equilibration. Reproduced with permission from Ref. [64], © Kröger, J. et al. 2020.

carrier separation, quantum-chemical calculations were employed to elucidate the role of triazine units in PHI. The models consist of a single pore of six imide-bridged heptazine units, both with and without melamine functionalization, were compared. In the non-functionalized model, excitons are delocalized across the heptazine units with interruptions at the imide bridges. Conversely, in the melamine-functionalized model, excitons become strongly localized at the heptazine unit adjacent to melamine. Since melamine is primarily located at the surface of PHI where photoinduced redox reactions occur, this localization is expected to enhance exciton separation and facilitate interaction with electron donors in solution. As shown in Figs. 12(d) and 12(e), the melamine group exhibits more hydrophobic behavior with water than heptazine units, evidenced by its sparser water molecule interaction and larger contact angle measurements. On the other hand, the surfactant and donor triethanolamine (TEOA) form strong hydrogen bonds with both melamine and heptazine, creating a catalyst-solution interface that facilitates charge transfer, donor oxidation and inhibits charge recombination (Figs. 12(b) and 12(c)). The above results all indicate that the presence of melamine units on the PHI surface provided a site for photoinduced redox reactions. The localization of charge carrier at this site could promote exciton separation and facilitate interaction with the electron donor in the solvent. In addition, the D–A heterostructure between heptazine and triazine also contributed to charge localization and separation. Hence, the surface-functionalized Mel-PHI exhibited an enhanced photocatalytic hydrogen evolution rate of 5570 μmol·h^{-1}·g^{-1} at optimized Pt loadings of 1.75 wt.% using TEOA as the electron donor. In comparison, K-PHI showed a significantly lower rate of 2200 μmol·h^{-1}·g^{-1} at an optimized 8 wt.% Pt loading, while the activity of H-PHI decreased further to 725 μmol·h^{-1}·g^{-1} at an optimized 2 wt.% Pt loading. The excellent photocatalytic hydrogen production performance of Mel-PHI can be attributed to several factors, including exciton localization, polarity, colloidal stability, wettability, efficient interfacial charge transfer and interaction with the sacrificial electron donor. This study demonstrated the potential of surface functionalization as a mean to adjust the photocatalytic properties of PHI.

PHI is an excellent photocatalyst for hydrogen production and possesses significant potential for the more challenging oxygen evolution reaction (OER), as demonstrated by Liu et al. [65]. DFT and time-dependent DFT (TD-DFT) calculations were utilized to assess the OER potential of PHI-M complexes (M = K$^+$, Rb$^+$, Mg^{2+}, Zn^{2+}, Co^{2+}, Mn^{2+}). Initial computational screening, using a periodic single PHI layer model doped with various metal cations, revealed that K$^+$ and Rb$^+$ localized in pore centers with weak interactions, while other metals preferred binding near charged nitrogen (Fig. 13(a)). Doping with metal cations can reduce the band gap by destabilizing the VB from hole localization around N atoms near the doping metal, while the CB mostly remains stable (Fig. 13(b)). As an exception, PHI-Zn^{2+} has the lowest conduction band position due to the filled d orbitals. The VB edges of Mg^{2+}, Zn^{2+}, Co^{2+} and

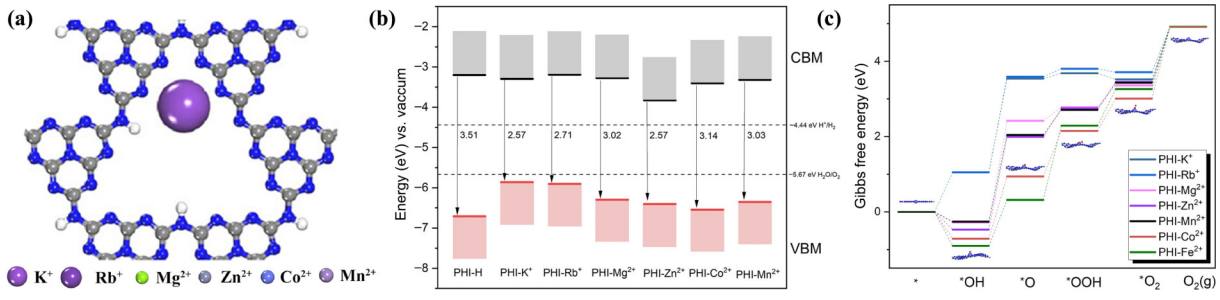

Figure 13 (a) DFT-optimized geometries of the single-layer PHI-M models. (b) Band position analysis for all PHI-M systems. (c) Simulated OER pathways for the series of metal-ion-doped PHI-M systems. Reproduced with permission from Ref. [65], © American Chemical Society 2024.

Mn^{2+} doped PHIs lie below O_2 oxidation potential, favoring hole and electron injection, while K^+ and Rb^+ doped PHIs are unfavorable due to relatively higher VB edge energy. Fig. 13(c) illustrates the simulated OER pathways for metal-ion-doped PHI-M systems, highlighting the potential as OER catalysts. Among the PHI-M system, PHI-Co^{2+} exhibits highly exothermic OH adsorption, which also implies the immense potential as OER catalyst. Bader charge analysis indicates that Mn^{2+} and Co^{2+} gain negative charges upon *OH adsorption, aligning with the highest stability due to highest calculated adsorption energies. Crystal orbital Hamilton population (COHP) further reveals strong Mn–O and Co–O bonding strengths, contributing to high intermediate stability. Additionally, TD-DFT analysis of PHI-M materials under light irradiation showed distinct absorption features linked to the charge of the metal cations. PHI-K^+ and PHI-Rb^+ displayed spectra similar to PHI-H, characterized by a shoulder at 3.5 eV. Divalent metal-doped PHIs showed red-shifted π–π* bands and new features in the low-energy region, with the exception of PHI-Mg^{2+}. PHI-Co^{2+} and PHI-Fe^{2+} exhibited the most significant low-energy absorption, with PHI-Co^{2+} displaying the most intense bands. It is anticipated that the simulated energy red-shift in the absorption features of the divalent metal cation PHI materials is linked to the photocatalytic activities, with the most substantial shift serving as evidence for the most promising predicted OER catalyst. To better validate the computational and theoretical predictions, the OER experiments with PHI-Co^{2+}, PHI-Fe^{2+}, PHI-K^+ and PHI-Mn^{2+} were conducted. Consistent with predictions, these experiments demonstrate that PHI-Co^{2+} has the highest OER performance with an oxygen production rate of 31.2 μmol·h^{-1}, nearly 60 times higher than g-C_3N_4 (0.5 μmol·h^{-1}) and surpassing WO_3/$BiVO_4$ (5 μmol·h^{-1}), while performing similarly to certain perovskites like $CaNbO_2N$ (40 μmol·h^{-1}).

Moreover, PHI demonstrates remarkable "photoelectronic storage" properties, with the utilization of this effect in dark photocatalytic reactions being initially documented by the same group in 2017 [86]. In the presence of sacrificial electron donors and sufficient illumination, PHI is capable of capturing exceptionally long-lived electrons, transitioning into an electron storage state. As depicted in Fig. 14(a), the color of polymer would change from yellow to blue when irradiated in the presence of electron donors. It was observed that the solution color gradually turned back to yellow after adding a hydrogen evolution cocatalyst to the irradiated solution in the dark in Fig. 14(b). In Fig. 14(d), the trapped electrons could be released as needed and utilized for generating hydrogen by introducing a Pt colloid in the dark, with a time delay of up to approximately 12 h. This observation demonstrated that the lifetime of the radical species exceeds the nocturnal duration, a phenomenon commonly referred to as 'dark photocatalysis'. Figure 14(c) illustrates that 'dark' photocatalysis is not observed in melon, highlighting the crucial involvement of the cyanamide moiety in radical generation. Combined with first-principles calculations, it was suggested that the presence of cyanamide moiety in PHI is essential for the photoelectronic storage characteristics. The long-time storage ability of trapped electrons of PHI provides a new approach to overcoming the limitation of the diurnal sunlight availability for photocatalyst. Further studies related to optimizing the properties of dark photocatalysts attracted researcher's interest, such as designing new PHI based hybrid light-harvesting and storing devices [53, 87]. The team further advanced the application of PHI as a direct photomemristive sensing platform, harnessing PHI's visible light bandgap, significant oxidation potential and inherent charge storage features [88]. They showcased memory sensing through charge accumulation and utilized potentiometric, impedimetric and coulometric readouts to write/erase information from the material by using the light-induced charge storage capability of K-PHI

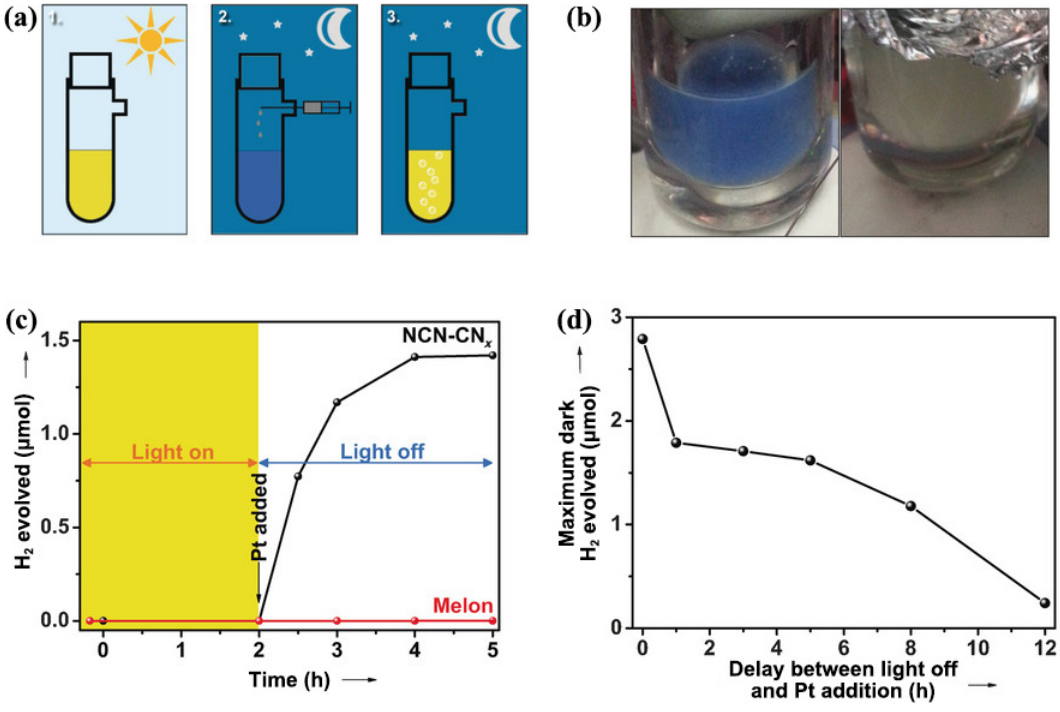

Figure 14 (a) Schematic diagram of the dark hydrogen evolution. (b) Photographs of the "blue radical" (left) and its color reversal subsequent to dark hydrogen evolution (right). (c) Comparison of dark hydrogen evolution of melon and NCN-CN_x. (d) Maximum dark hydrogen evolved as a function of the time between switching off the light and injection of the Pt colloid. Reproduced with permission from Ref. [86], © Lau, V. W. H. et al. 2016.

nanosheets. Furthermore, they demonstrated wireless colorimetric and fluorometric detection of the charging state of K-PHI nanoparticles, enabling the application as a particle-based autonomous sensing probe *in-situ*. PHI exhibited dual functionality, combining traditional PEC detection of various organic analytes with unique capabilities in light absorption, photocatalytic reactivity and charge storage. With these distinctive optoionic properties, the sensor can store sensing information and enable readouts based on physical parameters like photovoltage or color changes. This research introduced novel sensor functionalities by using PHI material, including memory of analyte concentration, adjustable sensitivities, dynamic sensing ranges and a versatile range of readout methods.

In addition to the applications mentioned above, heptazine-based materials have also been reported for therapeutic and environment-related applications. Many research groups have demonstrated the promising potential of carbon nitride materials in tumor therapy applications [86, 89, 90]. Xu et al. developed a NIR light-active red polymeric CN (RPCN) by thermally co-polymerizing melamine with a dopant with similar-structure, utilizing KCl as a template and potassium source [66]. The fine KCl particles effectively segregate the precursors, promoting the heterogeneous co-doping of carbon and potassium during high-temperature polycondensation processes. Additionally, at the interface between the precursors and KCl, the integration of K^+ ions and the release of Cl^- ions contribute to an alkaline environment that favors polymerization and facilitates the formation of heptazine rings. To further explore the electronic properties associated with the co-doping of C and K, DFT calculations were utilized to investigate the charge distributions in both pure PCN and RPCN (Fig. 15). The band structures and density of states (DOS) revealed that the lowest unoccupied molecular orbital (LUMO) is significantly influenced by C 2p and N 2p orbitals, while the highest occupied molecular orbital (HOMO) is primarily composed of N 2p orbitals in both materials. The DFT calculations clearly demonstrated that RPCN has a narrower bandgap than PCN,

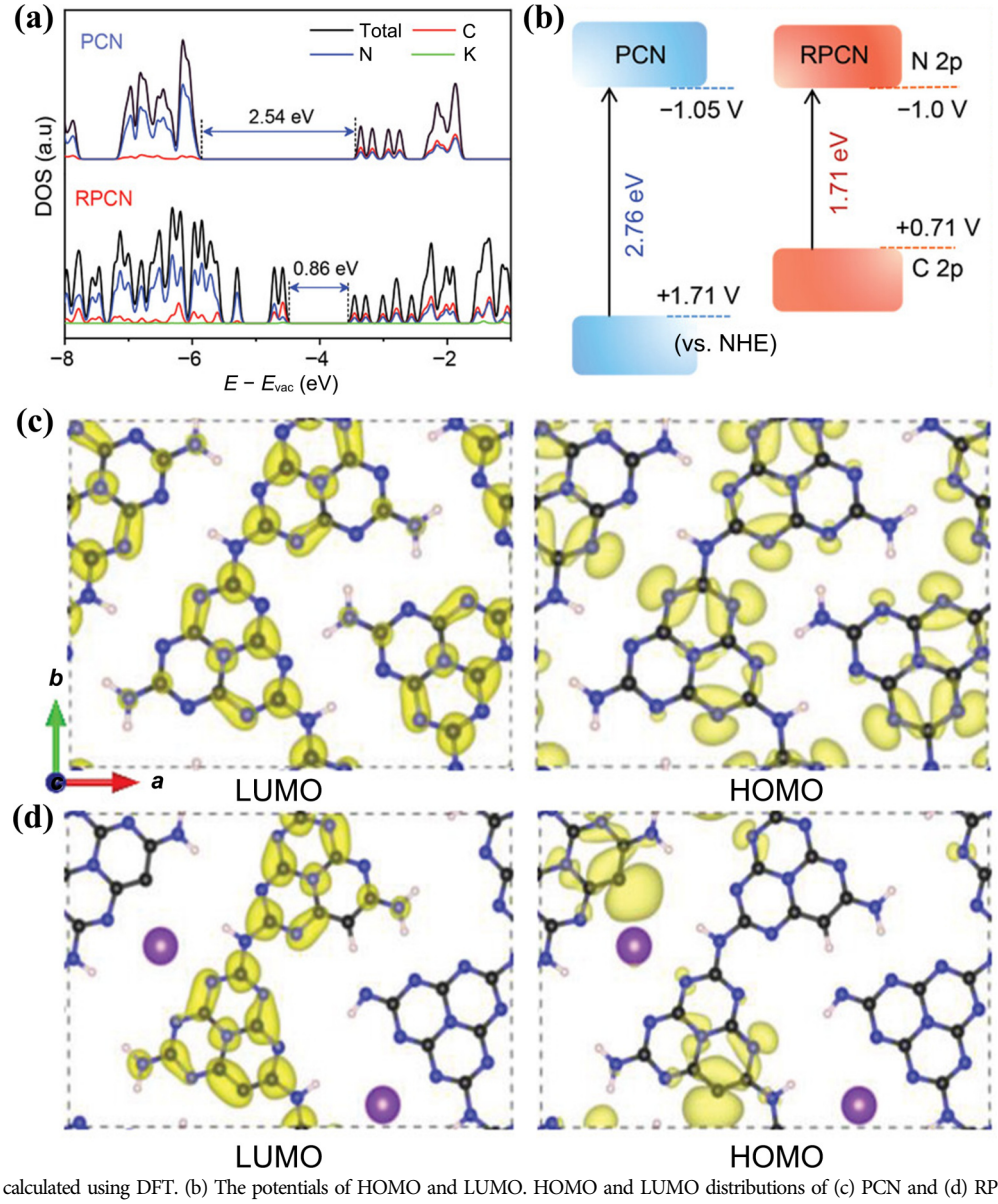

Figure 15 (a) DOS calculated using DFT. (b) The potentials of HOMO and LUMO. HOMO and LUMO distributions of (c) PCN and (d) RPCN. Reproduced with permission from Ref. [66], © Wiley-VCH GmbH 2021.

indicating an enhanced optical absorption range. Similarly, the results from the UV–vis–NIR absorption spectra and the transformed Kubelka–Munk (K–M) function plots reveal that the bandgap of PCN is 2.76 eV. In contrast, the synthesized RPCN, characterized by an upshifted valence band relative to PCN, exhibits a reduced bandgap of 1.71 eV, indicating an enhanced capacity for light absorption in the NIR region. As a result, RPCN not only exhibits the potential for hydrogen production under NIR illumination but also demonstrates the feasibility of employing near-infrared photocatalysis for hydrogen therapy in the biomedical field. A low power density of 0.5 $W \cdot cm^{-2}$ NIR irradiation (808 nm laser) was used to investigate the NIR photocatalytic hydrogen generation capability of RPCN in a glutathione (GSH) solution, abundant in the intratumoral microenvironment. The experiment demonstrated RPCN's high controllability and stability for NIR-responsive hydrogen generation. The anticancer performance of RPCN was further investigated *in vitro* and *in vivo* using a 4T1 tumor-bearing mice model. Following *in-situ* injection of RPCN, the hydrogen therapy group (RPCN + NIR) significantly inhibited 4T1 tumor growth over a 3-week treatment period due to intratumoral NIR-photocatalytic hydrogen generation and GSH depletion, thereby achieving efficient tumor therapy.

Furthermore, Wang's group achieved the synthesis of a highly ordered in-plane heptazine-based structure (PCNNS-IHO) for the mineralization of methyl mercaptan (CH_3SH) under visible light irradiation. This was accomplished through on-surface polymerization of melamine on the NaCl crystal surface at elevated temperatures [31]. The NaCl crystals, with the relatively high surface energy, could promote the adsorption and activation of melamine on the surface, thus effectively lowering the kinetic energy barrier of the condensation reaction. Moreover, the distinctive interaction between NaCl and melamine creates robust interfacial constraints, enabling the formation of 2D nanosheet structures on the NaCl surface. Additionally, NaCl serves as a reactant by doping Na^+ into the carbon nitride matrix, providing a strong structural base site for PCNNs-IHO. Due to the structural basicity, PCNNS-IHO exhibits excellent resistance to sulfation and recyclability for the mineralization of CH_3SH to SO_4^{2-} under visible light, outperforming bulk carbon nitride nanosheets and crystalline carbon nitride nanosheet. The CO_2 adsorption isotherm results indicate that PCNNS-IHO has a high density of basic sites, which enhances the ability to adsorb CH_3SH. To further investigate the adsorption of CH_3SH molecules on PCNNS-IHO, *in-situ* FT-IR spectroscopy was utilized. The analysis shows that, as the adsorption time of CH_3SH increases, the intensity of the negative peaks at 3400, 2180, 1160 and 960 cm^{-1} also rises. This increase suggests that the terminal amino groups, cyano groups and bridging nitrogen atoms of PCNNS-IHO function as active sites for the adsorption of CH_3SH. The outstanding properties of PCNNs-IHO indicate the potential for widespread applications in environmental purification and other fields.

3.3 Triazine-heptazine-based CCN

Although various strategies have been proposed to optimize the photocatalytic activity of CCN, the construction of BIEF is an effective approach to achieve optimal carrier separation. The building of heterojunctions between two semiconductors with suitable energy band levels has been demonstrated to be an effective approach to establish the BIEF for the efficient separation of photogenerated electron–hole pairs [91]. However, the abundant interface defects found in such heterojunctions can serve as recombination centers for photogenerated carriers, thereby weakening the photocatalytic effect [92]. To solve this issue, the heterostructure of homologous materials is preferred due to the similar physico-chemical properties [5, 93]. Hence, triazine-heptazine heterojunctions have been constructed to enhance photocatalytic activity. As previously mentioned, PHI consists of six heptazine units linked by –NH– bridges [53]. These interconnected units form a stacked arrangement with a large triangular gap capable of hosting a melamine molecule in the structure referred to as M-PHI, where M represents either a proton or a metal counterion [34, 37]. In contrast, PTI features a planar network of triazines connected by –NH– groups, with ions filling the interlayer spaces. The triazine rings in PTI exhibit an AB stacking configuration, creating uniform pore channels containing lithium halide ions (X^-), referred to as PTI/Li^+X^- [41]. The diverse pore sizes and chemical environments of nitrogen atoms significantly influences the energetic stabilities. Currently in PTI/PHI composite materials, PHI emerges as the thermodynamically preferred phase due to the exceptional stability. In contrast, PTI demonstrates metastable behavior under similar conditions [5]. Therefore, the heterointerface in PTI/PHI can form a unique D–A system [20]. First-principles calculations revealed that the energy band structure of PHI is more negative than PTI, facilitating notable charge transfer from PHI to PTI. This special D–A heterojunction configuration enhances the photocatalytic activity of this type of material by promoting faster electron migration rates [94]. Furthermore, as per the calculations conducted by Chang et al., the work function of PTI/PHI was notably lower at 3.35 eV compared to the individual values for pure PHI (4.56 eV) and PTI (4.20 eV). This finding suggests that the formation of the heterojunction substantially decreased the energy required for electron excitation [72]. The band structures of the heterostructure were in line with the conclusions drawn from the calculated work functions. Due to the unique characteristics of PTI/PHI, researchers have directed the focus towards investigating the synthesis methods required to construct such a heterojunction.

Li and co-workers synthesized heptazine and triazine-based crystalline CN (HTCN) by heating a mixture of preheated melamine and KCl/LiCl salts at 550 °C for 4 h under the air atmosphere [20]. The first principle confirms the stable stacking pattern of heptazine-based CN (HCN) and triazine-based CN (TCN) in the HTCN heterojunction. All three (HCN, TCN, HTCN) are direct bandgap semiconductors with the LUMO and the HOMO at the Γ point. HCN's LUMO and HOMO are slightly lower than TCN's, enabling HCN-TCN heterojunction formation (Figs. 16(b) and 16(e)). The value of HOMO and LUMO of HTCN together with DOS both demonstrate that the HOMO of HTCN derives from TCN and the LUMO of HTCN originates from HCN, which the heterojunction between HCN and TCN is of type II. Based on the experiment, they found that the product demonstrated optimal photocatalytic performance when melamine was preheated at 500 °C, they named it HTCN-500. Meanwhile, the ratio of HCN and TCN could be adjusted by controlling the preheated temperature of melamine, which further improves the photocatalytic efficiency. In Fig. 16(c), the lattice fringes of HTCN-500 are clearly displayed. These lattice fringes can be distinctly categorized into two sets: one measuring 0.33 nm, which corresponds to HCN and the other measuring 0.29 nm, associated with TCN. This finding further provides evidence supporting the composite nature of HTCN-500, which incorporates both HCN and TCN structures. These observations are consistent with results

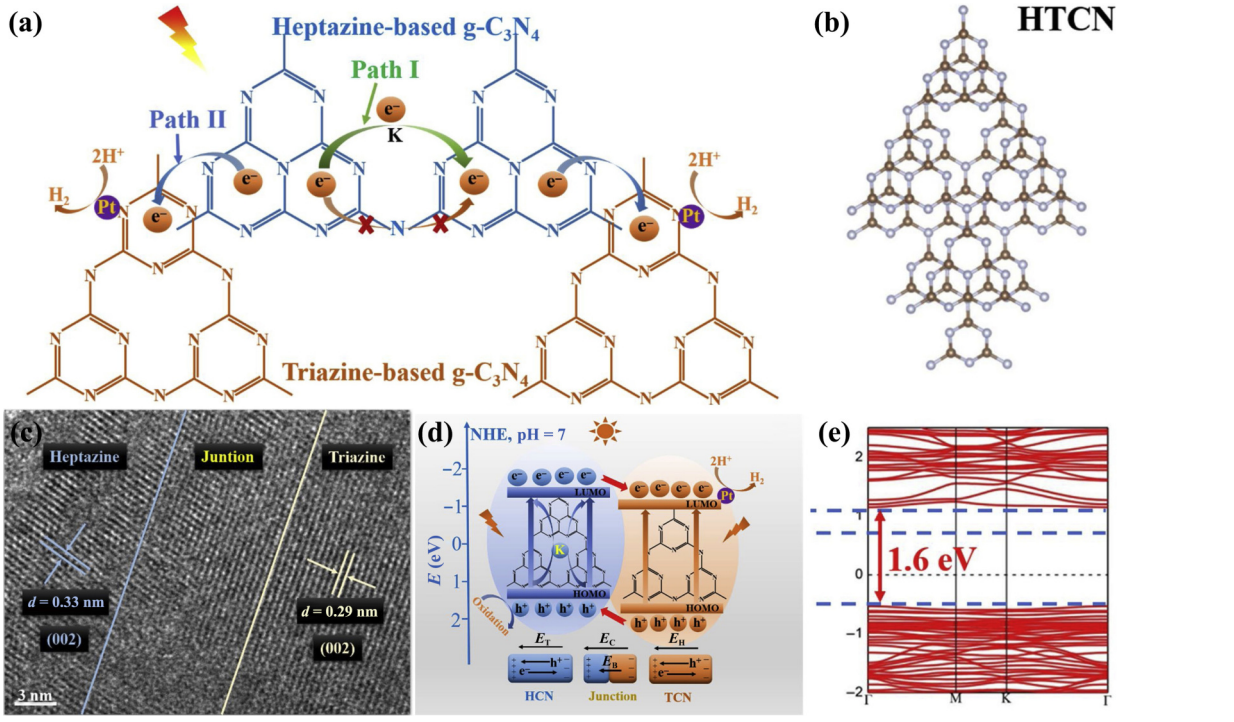

Figure 16 (a) Electron transfer process of HTCN. (b) The optimized stacking patterns of HTCN. (c) HR-TEM image of HTCN-500. (d) The photocatalytic mechanisms of HTCN under light irradiation: E_C is the contact electric field for the two materials; E_B is the potential barrier in the interfacial ($E_B < E_C$ during the photocatalytic reaction); E_H and E_T are the internal electric fields induced by the redistribution of the spatial charges in HCN and TCN, respectively. (e) The band structures of HTCN. Reproduced with permission from Ref. [20], © Elsevier B.V. 2019.

obtained from XRD, diffuse reflectance spectroscopy (DRS) and scanning electron microscopy (SEM) analyses. The HR-TEM also showed the interface of triazine and heptazine with less crystalline, possibly owing to mismatched molecular structure. The X-ray photoelectron spectroscopy (XPS) spectra showed the existence of K in HCN and HTCN-500. The K^+ ions could provide delivery paths for photo-induced carriers among adjacent heptazine units. Based on the hydrogen evolution reaction (HER) comparison experiments, the larger π-conjugated system of HCN in the heptazine unit facilitates better electron transfer, resulting in a higher HER in comparison with HCN and reference GCN derived from traditional pyrolysis. The HTCN-500 samples demonstrate the best HER, underscoring the critical role of the HCN-TCN heterojunction in boosting photocatalytic activity. A mechanism for hydrogen evolution in HTCN-500 is proposed, where the staggered band gap of the heterojunction benefited the transfer of photo-induced electrons between heptazine and triazine units, as shown in Fig. 16(d). Two primary pathways for photogenerated electrons are identified in Fig. 16(a). First, K^+ ions intercalated in the heptazine unit create pathways that improve electronic delocalization and extend π-conjugated systems. The second pathway involves electron transfer facilitated by the heterojunction between heptazine and triazine units. This mechanism provides strong support for the enhanced photocatalytic activity of HTCN and the verification of experimental results has further reinforced this point, demonstrating that the HTCN exhibits the most superior photocatalytic performance. The HTCN showed the highest photocatalytic H_2 evolution rate of 890 μmol·h^{-1}·g^{-1}, which was 15, 8 and 1.6 times higher than that of GCN, TCN and HCN, respectively.

Sun et al. prepared an omasum-like crystalline CCN array (MA-rod array) featuring triazine–heptazine heterojunctions through sequential molecule self-assembly followed by a molten salt-assisted polycondensation process [73]. The solvation and coordination effects of a eutectic mixture (LiCl/KCl) led to the formation of the array structure. The CCN array exhibited the optimal hydrogen production rate of 11.720 mmol·h^{-1}·g_{cat}^{-1} with an apparent quantum yield of 60% at 420 nm, which surpassed the reference GCN by 51 times. DFT calculations were conducted to explore the electronic configuration of MA-rod array. The product displays a higher DOS at the triazine–heptazine hetero-interface particularly near the CB edges, compared to the reference melamine-derived PTI and is similar to the melamine-derived PHI. This result suggests that the heptazine units contribute to an increased electron density in the conduction band. The calculated electron density of HOMO and LUMO for the MA-rod array indicates that the electron densities at the hetero-interface is inhomogenous. Such inhomogeneity can facilitate electronic disturbance, thereby promoting the directed migration of charge carriers. The D–A system formed within the triazine–heptazine heterojunction can speed up the migration of charge carriers while suppressing electron–hole recombination, ultimately enhancing photocatalytic activity [95, 96]. The results of PL and electrochemical impedance spectroscopy (EIS) indicated a high mobility of photogenerated carriers within the array. The unique array configuration, rapid electrolyte diffusion, fast electronic transmission, low interface resistance and fast charge carriers migration all contributed to the remarkable photocatalytic activity.

Except for KCl/LiCl, recent studies by Zhang and coworkers have shown that NaCl/KCl could also be used as an alternative eutectic salt to construct triazine–heptazine-based D–A heterostructures [29]. The higher melting point of NaCl/KCl leads to a partial transformation from heptazine to triazine, resulting in a more robust triazine–heptazine-based structure with high activity.

Despite the lower crystallinity and optical absorption, CN-NaK has proven to be the most efficient photocatalytic hydrogen evolution among various copolymers synthesized using different eutectic salts. In another study by Chang et al., a facile one-pot salt fog thermal polymerization method was employed to produce a porous carbon nitride nanosheet with a triazine–heptazine heterostructure using NaCl/KCl [72]. This method differs from the traditional molten salt method, as it involves dissolving urea in an aqueous solution of NaCl/KCl rather than using solid salts. The thermal polymerization reaction was initiated under a salt fog environment by gradually heating the mixed solution to 550 °C in a muffle furnace. The salt fog, generated by the combination of molten salts with water vapor during the thermal polymerization process, helps mitigate the negative effects of pure molten salt-assisted thermal methods, leading to a product with a large amount of mesopores. UV–vis DRS measurements confirm a notably enhanced light absorption capacity for the product, accompanied by a visible red shift in the absorption edge. Such observation suggests an improved utilization of visible light and an increased photogenerated carrier yield compared to references. The formation of intermolecular heptazine/triazine heterostructure effectively minimizes the band gap compared to individual constituents. Theoretical calculations further elucidate the advantage of this heterostructure over pure heptazine and triazine, as electrons preferentially migrate from triazine to heptazine unit upon contact, forming a type II heterojunction. This junction creates a built-in electric field and a reduced work function (3.35 eV), facilitating electron excitation and enhancing interfacial charge transfer. Consequently, the triazine/heptazine intermolecular heterostructure holds promise in promoting the photocatalytic activity. The adsorption energy and Gibbs free energy for hydrogen evolution reduction on various N-sites in triazine/heptazine heterostructure were calculated to identify optimal sites (Fig. 17(b)). Results show that the 5 examined sites possess negative energies, enabling spontaneous hydrogen

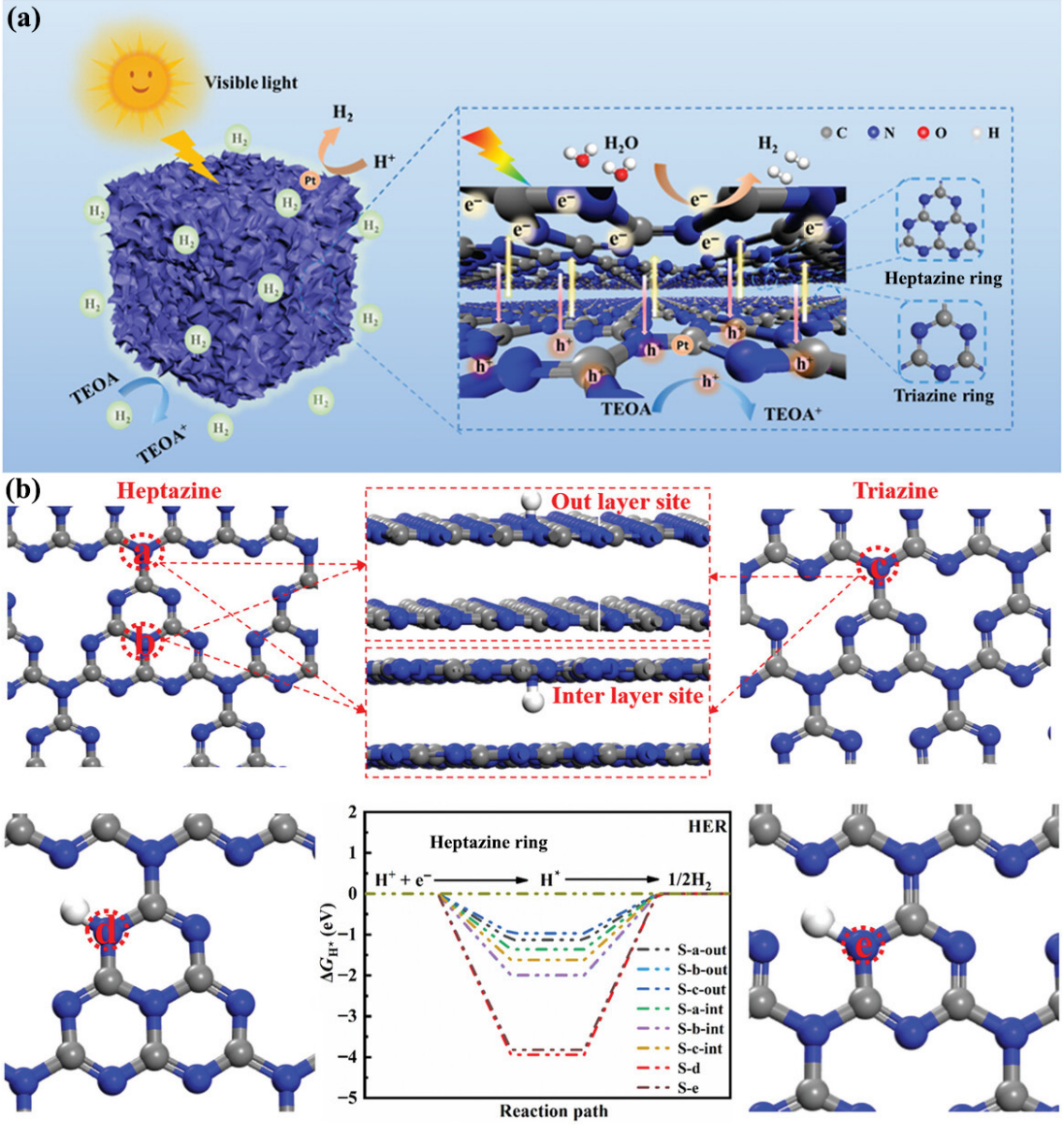

Figure 17 (a) The schematic illustration of the working mechanism. (b) The calculated Gibbs free energy for the hydrogen evolution reaction at various N-sites, indicated by red dashed circles, within the triazine/heptazine heterostructure. Reproduced with permission from Ref. [72], © Wiley-VCH GmbH 2023.

generation under visible light. Notably, the N atoms at site d in heptazine exhibit the most favorable conditions for hydrogen adsorption and production due to the lowest calculated Gibbs free energy of −0.39 eV. Additionally, the hydrophilic nature of oxygenated C_3N_4 layers allows rapid dispersion in water, enabling the materials with relatively low specific surface areas to achieve notably high photocatalytic hydrogen evolution rates, surpassing those of materials with larger surface areas. Based on the working mechanism depicted in Fig. 17(a), the fabricated porous SF-CN_{1-3} exhibited an exceptional photocatalytic activity. It showed the highest photocatalytic hydrogen evolution rate of approximately 18.18 mmol·h^{-1}·g^{-1}, up to 259 times that of pristine g-C_3N_4. The high activity of SF-CN_{1-3} was attributed to the enlarged specific surface area, enhanced absorption of visible light, narrow band gap and increased photocurrent response.

Zhang et al. fabricated a hybrid PHI/PTI copolymer with semi-coherent interfaces via a two-step salt-melt synthetic process [74]. Initially, melamine was utilized to synthesize an amorphous copolymer of heptazine–triazine in the presence of $CaCO_3$. This oligomer was further polymerized into a fully condensed PHI/PTI in a LiCl/KCl environment. The XRD spectrum of the product clearly shows prominent peaks at 8° and 28°, which correspond to the in-plane repeating packing and interlayer stacking distance of heptazine units, characteristic of typical PHI. The diffraction peaks at 12°, 21°, 26°, 29° and so on are related to PTI. These results suggested the successful synthesis of a copolymer containing both PHI and PTI units. The FTIR and Raman spectra further proved the existence of heptazine and triazine units. The SEM image of PHI/PTI reveals a typical nanorod structure of PHI and a few hexagonal prisms that are likely derived from PTI. The semi-coherent interface structure between PHI and PTI enables the rapid transfer of charge carriers across the junction, which was further explored by DFT calculations. A semi-coherent PHI $(2\bar{1}\bar{1}0)$–PTI $(10\bar{1}0)$ interface was formed, presenting a 0.42 eV potential difference, with the $(10\bar{1}0)$ plane of PHI epitaxially to the $(10\bar{1}0)$ plane of PTI. The average charge density difference map of PHI/PTI shows electron accumulation near PHI and depletion near PTI, creating a built-in field favoring electron transfer from PHI to PTI. Upon exposure to visible light, PHI is excited to generate electron–hole pairs. The excited electrons are efficiently transferred to the conduction band of PTI, facilitated by a well-established built-in electric field with a low energy barrier, thereby enhancing the efficient separation of photogenerated electrons and holes. As a result, the PHI/PTI copolymer demonstrates an enhanced photocatalytic hydrogen production efficiency at 348.5 μmol·h^{-1}, which is 7.9 greater than that of PHI (44 μmol·h^{-1}) and approximately 64 higher than that of melon (5.4 μmol·h^{-1}).

4 Summary and outlook

To date, numerous methodologies have been devised to synthesize CCNs. Due to the remarkably low defect concentration, CCNs exhibit unparalleled photon-induced charge transport efficiency and sluggish recombination kinetics for electron–hole pairs. Furthermore, the optical absorbance of the CCNs is considerably superior to that of melon-derived GCN, arising from the elongated π-conjugated system and elevated stiffness of the conjugated polymer backbone. These characteristics contribute to the enhanced photocatalytic activity relative to melon-derived GCN. Therefore, CCNs represent an innovative class of conjugated photocatalysts for water dissociation and other photo-induced transformations, such as CO_2 photoreduction and organic photosynthesis. The high degree of crystallinity and the precise structural configuration may render these CCNs applicable as model systems for studying photocatalytic processes in conjugated semiconductors.

Beyond fundamental research, the potential applications of CCNs are extensive and diverse, particularly in solar energy conversion technologies, enabling devices to harness sunlight more efficiently. In photocatalytic fuel cells, CCNs could enable the direct conversion of sunlight into storable energy forms. Additionally, the integration into semiconductor-based (photo) electrocatalytic systems may lead to more efficient and sustainable electrochemical processes. CCNs also show promise as highly sensitive sensors, paving the way for innovative advancements in optoelectronics and display technologies. In summary, CCNs are regarded as a promising class of materials that encompass a wide range of fields, from energy conversion to sensing and optoelectronics. However, there are still some challenges that need to be explored:

(1) While it is widely acknowledged that low-melting-point molten salts primarily facilitate crystallization reactions through the solvating effects and that high-melting-point molten salts are primarily regarded as templates in the formation of CCNs, the specific influence and mechanism of different molten salts on the crystallinity of CCNs remains not very clear. Additionally, the currently reported synthetic methods face the issue of excessive molten salt usage, leading to significant waste. Therefore, it is crucial to explore low-dose molten salt-assisted synthesis of CCN and to investigate new mechanisms.

(2) While alkali chlorides are most frequently used due to their favorable melting points, excellent chemical stability and high electrical conductivity, which facilitate the ordered arrangement of carbon nitride precursors, the research on exploring alternative salts for CCN synthesis is still limited. Exploring the anions in molten salts may provide new possibilities for the polymerization pathways of CCN, potentially further expanding the variety and applications of molten salts.

(3) The structure of precursors after calcination is generally two-dimensional and the development of new synthetic methods for preparing three-dimensional nanostructure has received scant attention.

(4) The small crystallite size of CCN poses difficulties in structural analysis and the sensitivity to the electron beam makes it hard to use traditional HR-TEM for atom structure analysis. Another reason is the lack of methods for producing high-quality CCN. Most currently synthesized CCNs exhibit certain defects and relatively large thicknesses, which complicate high-quality electron microscopy characterization. Although DPC-STEM technology has matured and made significant contributions to the atomic structure characterization of PTI, the application for the structural analysis of PHI is still relatively limited. Obtaining complete atomic structural information is crucial for exploring the relationship between structure and properties. Based on this, studying the local defects and the positioning, structure and distribution of doped elements can further reveal the potential mechanisms of catalysis.

(5) Currently, the exploration and utilization of PTI mainly focus on photocatalytic reactions. However, the limited light absorption capacity restricts PTI to activation primarily by UV light, significantly hindering its practical applicability. In addition to improving light absorption through molecular engineering and structural optimization, it is equally important to identify innovative applications for PTI.

(6) There are few reports on the use of PHI for overall water

splitting. On the other hand, PTI shows a crystal face-dependent overall water-splitting activity. At the same time, some modified amorphous GCNs also demonstrate the ability for complete water splitting. This suggests that, whether amorphous or crystalline, some undiscovered factors may determine the water-splitting performance of carbon nitride materials [97]. New mechanisms still need to be explored to enrich the theory of the carbon nitride family in water splitting.

In summary, future studies related to the mechanism exploration, method optimization and application expansion are still necessary for CCNs. The atomic and defective structure information of CCN is also crucial depending on the advanced technology, such as DPC-STEM and scanning tunneling spectroscopy (STM). With the new strategies, it could be possible to identify the location of defects and heteroatoms within the CCN network and establish relationships with the performance, which may contribute to more photocatalytic applications with high efficiency.

Data availability

Not applicable.

Acknowledgements

This work was financially supported by the Science, Technology and Innovation Commission of Shenzhen Municipality (No. JCYJ20220818100212027), Guangdong Provincial Key Laboratory of Energy Materials for Electric Power (No. 2018B030322001), Guangdong Provincial Key Laboratory of Catalysis (No. 2020B121201002) and Guangdong Province Ordinary University Innovation Team Project (No. 2024KCXTD063). This work was supported by the Pico Center at SUSTech, which received support from a Presidential fund and the Development and Reform Commission of Shenzhen Municipality.

Declaration of competing interest

All the contributing authors report no conflict of interests in this work.

Author contribution statement

Y. Y. T.: Conceptualization, investigation, data curation, formal analysis, visualization, writing – original draft. Z. Y. Z.: Investigation, data curation. Y. Y. P.: Resources. Z. Z. S.: Conceptualization, writing – review & editing. L. M. H.: Funding acquisition, project administration, supervision, writing – review & editing. All the authors have approved the final manuscript.

Use of AI statement

None.

References

[1] Fujishima, A.; Honda, K. Electrochemical photolysis of water at a semiconductor electrode. *Nature* **1972**, *238*, 37–38.

[2] Maeda, K.; Teramura, K.; Lu, D. L.; Takata, T.; Saito, N.; Inoue, Y.; Domen, K. Photocatalyst releasing hydrogen from water. *Nature* **2006**, *440*, 295–295.

[3] Wang, X. C.; Maeda, K.; Thomas, A.; Takanabe, K.; Xin, G.; Carlsson, J. M.; Domen, K.; Antonietti, M. A metal-free polymeric photocatalyst for hydrogen production from water under visible light. *Nat. Mater.* **2009**, *8*, 76–80.

[4] Burrow, J. N.; Ciufo, R. A.; Smith, L. A.; Wang, Y.; Calabro, D. C.; Henkelman, G.; Mullins, C. B. Calcium poly(heptazine imide): A covalent heptazine framework for selective CO_2 adsorption. *ACS Nano* **2022**, *16*, 5393–5403.

[5] Zheng, Y.; Lin, L. H.; Wang, B.; Wang, X. C. Graphitic carbon nitride polymers toward sustainable photoredox catalysis. *Angew. Chem., Int. Ed.* **2015**, *54*, 12868–12884.

[6] Ong, W. J.; Tan, L. L.; Ng, Y. H.; Yong, S. T.; Chai, S. P. Graphitic carbon nitride ($g\text{-}C_3N_4$)-based photocatalysts for artificial photosynthesis and environmental remediation: Are we a step closer to achieving sustainability. *Chem. Rev.* **2016**, *116*, 7159–7329.

[7] Sun, X. J.; Yang, D. D.; Dong, H.; Meng, X. B.; Sheng, J. L.; Zhang, X.; Wei, J. Z.; Zhang, F. M. ZIF-derived CoP as a cocatalyst for enhanced photocatalytic H_2 production activity of $g\text{-}C_3N_4$. *Sustain. Energy Fuels* **2018**, *2*, 1356–1361.

[8] Li, Y.; Li, B. H.; Zhang, D. N.; Cheng, L.; Xiang, Q. J. Crystalline carbon nitride supported copper single atoms for photocatalytic CO_2 reduction with nearly 100% CO selectivity. *ACS Nano* **2020**, *14*, 10552–10561.

[9] Lin, Y.; Su, W. Y.; Wang, X. X.; Fu, X. Z.; Wang, X. C. LaOCl-coupled polymeric carbon nitride for overall water splitting through a one-photon excitation pathway. *Angew. Chem., Int. Ed.* **2020**, *59*, 20919–20923.

[10] Li, Y.; Zhang, D. N.; Feng, X. H.; Xiang, Q. J. Enhanced photocatalytic hydrogen production activity of highly crystalline carbon nitride synthesized by hydrochloric acid treatment. *Chin. J. Catal.* **2020**, *41*, 21–30.

[11] Zhang, M. M.; Lai, C.; Li, B. S.; Huang, D. L.; Zeng, G. M.; Xu, P.; Qin, L.; Liu, S. Y.; Liu, X. G.; Yi, H. et al. Rational design 2D/2D $BiOBr/CDs/g\text{-}C_3N_4$ Z-scheme heterojunction photocatalyst with carbon dots as solid-state electron mediators for enhanced visible and NIR photocatalytic activity: Kinetics, intermediates, and mechanism insight. *J. Catal.* **2019**, *369*, 469–481.

[12] Chen, J. L.; Hong, Z. H.; Chen, Y. L.; Lin, B. Z.; Gao, B. F. One-step synthesis of sulfur-doped and nitrogen-deficient $g\text{-}C_3N_4$ photocatalyst for enhanced hydrogen evolution under visible light. *Mater. Lett.* **2015**, *145*, 129–132.

[13] Sun, Z. Z.; Wang, W.; Chen, Q. W.; Pu, Y. Y.; He, H.; Zhuang, W. M.; He, J. Q.; Huang, L. M. Hierarchical carbon nitride tube with oxygen doping and carbon defects promotes solar-to-hydrogen conversion. *J. Mater. Chem. A* **2020**, *8*, 3160–3167.

[14] Lin, L. H.; Lin, Z. Y.; Zhang, J.; Cai, X.; Lin, W.; Yu, Z. Y.; Wang, X. C. Molecular-level insights on the reactive facet of carbon nitride single crystals photocatalysing overall water splitting. *Nat. Catal.* **2020**, *3*, 649–655.

[15] Chen, X. X.; Cai, X.; Li, Y.; Zhang, Y. F.; Lin, W. Effects of potassium ions and platinum cocatalysts on the photocatalytic performance of poly(heptazine imides). *Appl. Surf. Sci.* **2023**, *639*, 158275.

[16] Bojdys, M. J.; Müller, J. O.; Antonietti, M.; Thomas, A. Ionothermal synthesis of crystalline, condensed, graphitic carbon nitride. *Chem.—Eur. J.* **2008**, *14*, 8177–8182.

[17] Ham, Y.; Maeda, K.; Cha, D.; Takanabe, K.; Domen, K. Synthesis and photocatalytic activity of poly(triazine imide). *Chem.—Asian J.* **2013**, *8*, 218–224.

[18] Lin, L. H.; Ou, H. H.; Zhang, Y. F.; Wang, X. C. Tri-*s*-triazine-based crystalline graphitic carbon nitrides for highly efficient hydrogen evolution photocatalysis. *ACS Catal.* **2016**, *6*, 3921–3931.

[19] Algara-Siller, G.; Severin, N.; Chong, S. Y.; Björkman, T.; Palgrave, R. G.; Laybourn, A.; Antonietti, M.; Khimyak, Y. Z.; Krasheninnikov, A. V.; Rabe, J. P. et al. Triazine-based graphitic carbon nitride: A two-dimensional semiconductor. *Angew. Chem., Int. Ed.* **2014**, *53*, 7450–7455.

[20] Li, Y.; Gong, F.; Zhou, Q.; Feng, X. H.; Fan, J. J.; Xiang, Q. J.

Crystalline isotype heptazine-/triazine-based carbon nitride heterojunctions for an improved hydrogen evolution. *Appl. Catal. B: Environ.* **2020**, *268*, 118381.

[21] Song, H. J.; Luo, L. Y.; Wang, S. Y.; Zhang, G.; Jiang, B. J. Advances in poly(heptazine imide)/poly(triazine imide) photocatalyst. *Chin. Chem. Lett.* **2024**, *35*, 109347.

[22] Zhao, B. B.; Zhong, W.; Chen, F.; Wang, P.; Bie, C. B.; Yu, H. G. High-crystalline g-C_3N_4 photocatalysts: Synthesis, structure modulation, and H_2-evolution application. *Chin. J. Catal.* **2023**, *52*, 127–143.

[23] Fang, Y. X.; Hou, Y. D.; Fu, X. Z.; Wang, X. C. Semiconducting polymers for oxygen evolution reaction under light illumination. *Chem. Rev.* **2022**, *122*, 4204–4256.

[24] Lin, L. H.; Yu, Z. Y.; Wang, X. C. Crystalline carbon nitride semiconductors for photocatalytic water splitting. *Angew. Chem., Int. Ed.* **2019**, *58*, 6164–6175.

[25] Liu, J. J.; Fu, W.; Liao, Y. L.; Fan, J. J.; Xiang, Q. J. Recent advances in crystalline carbon nitride for photocatalysis. *J. Mater. Sci. Technol.* **2021**, *91*, 224–240.

[26] Zhao, Z. L.; Shu, Z.; Zhou, J.; Ye, L. N.; Li, T. T.; Wang, W. B.; Xu, L. N. NH-rich red poly(heptazine imide) nanoparticles with simultaneously promoted exciton dissociation and activated n → π* electronic transition for boosted photocatalytic H_2 generation. *J. Mater. Chem. A* **2022**, *10*, 17668–17679.

[27] Yan, X.; Li, J. T.; Zhou, H. F. Molten salts synthesis and visible light photocatalytic activity of crystalline poly(triazine imide) with different morphologies. *J. Mater. Sci. Mater. Electron.* **2019**, *30*, 11706–11713.

[28] Wang, W. B.; Shu, Z.; Liao, Z. H.; Zhou, J.; Meng, D. W.; Li, T. T.; Zhao, Z. L.; Xu, L. N. Sustainable one-step synthesis of nanostructured potassium poly(heptazine imide) for highly boosted photocatalytic hydrogen evolution. *Chem. Eng. J.* **2021**, *424*, 130332.

[29] Zhang, G. G.; Lin, L. H.; Li, G. S.; Zhang, Y. F.; Savateev, A.; Zafeiratos, S.; Wang, X. C.; Antonietti, M. Ionothermal synthesis of triazine–heptazine-based copolymers with apparent quantum yields of 60% at 420 nm for solar hydrogen production from "sea water." *Angew. Chem., Int. Ed.* **2018**, *57*, 9372–9376.

[30] Lau, V. W. H.; Moudrakovski, I.; Botari, T.; Weinberger, S.; Mesch, M. B.; Duppel, V.; Senker, J.; Blum, V.; Lotsch, B. V. Rational design of carbon nitride photocatalysts by identification of cyanamide defects as catalytically relevant sites. *Nat. Commun.* **2016**, *7*, 12165.

[31] Guo, F. S.; Hu, B.; Yang, C.; Zhang, J. S.; Hou, Y. D.; Wang, X. C. On-surface polymerization of in-plane highly ordered carbon nitride nanosheets toward photocatalytic mineralization of mercaptan gas. *Adv. Mater.* **2021**, *33*, 2101466.

[32] Qiu, C. T.; Xu, Y. S.; Fan, X.; Xu, D.; Tandiana, R.; Ling, X.; Jiang, Y. N.; Liu, C. B.; Yu, L.; Chen, W. et al. Highly crystalline K-intercalated polymeric carbon nitride for visible-light photocatalytic alkenes and alkynes deuterations. *Adv. Sci.* **2019**, *6*, 1801403.

[33] Xu, Y. S.; He, X.; Zhong, H.; Singh, D. J.; Zhang, L. J.; Wang, R. H. Solid salt confinement effect: An effective strategy to fabricate high crystalline polymer carbon nitride for enhanced photocatalytic hydrogen evolution. *Appl. Catal. B: Environ.* **2019**, *246*, 349–355.

[34] Bhunia, M. K.; Yamauchi, K.; Takanabe, K. Harvesting solar light with crystalline carbon nitrides for efficient photocatalytic hydrogen evolution. *Angew. Chem., Int. Ed.* **2014**, *53*, 11001–11005.

[35] Chong, S. Y.; Jones, J. T. A.; Khimyak, Y. Z.; Cooper, A. I.; Thomas, A.; Antonietti, M.; Bojdys, M. J. Tuning of gallery heights in a crystalline 2D carbon nitride network. *J. Mater. Chem. A* **2013**, *1*, 1102–1107.

[36] Li, J. Y.; Barrio, J.; Fang, Y. X.; Pan, Y. X.; Volokh, M.; Mondal, S.; Tzadikov, J.; Abisdris, L.; Tashakory, A.; Wang, X. C. et al. Elucidating the effect of crystallinity on the photoactivity in poly(heptazine imides). *Energy Fuels* **2023**, *37*, 18145–18153.

[37] Zhang, G. G.; Li, G. S.; Heil, T.; Zafeiratos, S.; Lai, F. L.; Savateev, A.; Antonietti, M.; Wang, X. C. Tailoring the grain boundary chemistry of polymeric carbon nitride for enhanced solar hydrogen production and CO_2 reduction. *Angew. Chem., Int. Ed.* **2019**, *58*, 3433–3437.

[38] Zhang, G. Q.; Huang, W.; Xu, Y. S.; Li, Y. L.; He, C. X.; Ren, X. Z.; Zhang, P. X.; Mi, H. W. Suppressing defects-induced non-radiative recombination for activating the near-infrared photoactivity of red polymeric carbon nitride. *Adv. Funct. Mater.* **2023**, *33*, 2305935.

[39] Fettkenhauer, C.; Clavel, G.; Kailasam, K.; Antonietti, M.; Dontsova, D. Facile synthesis of new, highly efficient SnO_2/carbon nitride composite photocatalysts for the hydrogen evolution reaction. *Green Chem.* **2015**, *17*, 3350–3361.

[40] Wang, Q.; Zhang, G. G.; Xing, W. D.; Pan, Z. M.; Zheng, D. D.; Wang, S. B.; Hou, Y. D.; Wang, X. C. Bottom-up synthesis of single-crystalline poly (triazine imide) nanosheets for photocatalytic overall water splitting. *Angew. Chem.* **2023**, *135*, e202307930.

[41] Shao, Y. F.; Hao, X. Q.; Lu, S. D.; Jin, Z. L. Molten salt-assisted synthesis of nitrogen-vacancy crystalline graphitic carbon nitride with tunable band structures for efficient photocatalytic overall water splitting. *Chem. Eng. J.* **2023**, *454*, 140123.

[42] Tian, L.; Li, J. Y.; Liang, F.; Wang, J. K.; Li, S. S.; Zhang, H. J.; Zhang, S. W. Molten salt synthesis of tetragonal carbon nitride hollow tubes and their application for removal of pollutants from wastewater. *Appl. Catal. B: Environ.* **2018**, *225*, 307–313.

[43] Ou, H. H.; Yang, P. J.; Lin, L. H.; Anpo, M.; Wang, X. C. Carbon nitride aerogels for the photoredox conversion of water. *Angew. Chem., Int. Ed.* **2017**, *56*, 10905–10910.

[44] Yuan, J. L.; Tang, Y. H.; Yi, X. Y.; Liu, C. B.; Li, C.; Zeng, Y. X.; Luo, S. L. Crystallization, cyanamide defect and ion induction of carbon nitride: Exciton polarization dissociation, charge transfer and surface electron density for enhanced hydrogen evolution. *Appl. Catal. B: Environ.* **2019**, *251*, 206–212.

[45] Li, X. C.; Chen, X. X.; Fang, Y. X.; Lin, W.; Hou, Y. D.; Anpo, M.; Fu, X. Z.; Wang, X. C. High-performance potassium poly(heptazine imide) films for photoelectrochemical water splitting. *Chem. Sci.* **2022**, *13*, 7541–7551.

[46] Xia, P. F.; Cheng, B.; Jiang, J. Z.; Tang, H. Localized π-conjugated structure and EPR investigation of g-C_3N_4 photocatalyst. *Appl. Surf. Sci.* **2019**, *487*, 335–342.

[47] McDermott, E. J.; Wirnhier, E.; Schnick, W.; Virdi, K. S.; Scheu, C.; Kauffmann, Y.; Kaplan, W. D.; Kurmaev, E. Z.; Moewes, A. Band gap tuning in poly(triazine imide), a nonmetallic photocatalyst. *J. Phys. Chem. C* **2013**, *117*, 8806–8812.

[48] Li, X. H.; Zhang, J. S.; Chen, X. F.; Fischer, A.; Thomas, A.; Antonietti, M.; Wang, X. C. Condensed graphitic carbon nitride nanorods by nanoconfinement: Promotion of crystallinity on photocatalytic conversion. *Chem. Mater.* **2011**, *23*, 4344–4348.

[49] Xiong, T.; Cen, W. L.; Zhang, Y. X.; Dong, F. Bridging the g-C_3N_4 interlayers for enhanced photocatalysis. *ACS Catal.* **2016**, *6*, 2462–2472.

[50] Wang, W.; Cui, J.; Sun, Z. Z.; Xie, L.; Mu, X. K.; Huang, L. M.; He, J. Q. Direct atomic-scale structure and electric field imaging of triazine-based crystalline carbon nitride. *Adv. Mater.* **2021**, *33*, 2106359.

[51] Shen, B. Y.; Chen, X.; Shen, K.; Xiong, H.; Wei, F. Imaging the node-linker coordination in the bulk and local structures of metal-organic frameworks. *Nat. Commun.* **2020**, *11*, 2692.

[52] Shen, B. Y.; Chen, X.; Cai, D. L.; Xiong, H.; Liu, X.; Meng, C. G.; Han, Y.; Wei, F. Atomic spatial and temporal imaging of local structures and light elements inside zeolite frameworks. *Adv. Mater.* **2020**, *32*, 1906103.

[53] Schlomberg, H.; Kröger, J.; Savasci, G.; Terban, M. W.; Bette, S.; Moudrakovski, I.; Duppel, V.; Podjaski, F.; Siegel, R.; Senker, J. et al. Structural insights into poly(heptazine imides): A light-storing carbon nitride material for dark photocatalysis. *Chem. Mater.* **2019**, *31*, 7478–7486.

[54] da Silva, M. A. R.; Silva, I. F.; Xue, Q.; Lo, B. T. W.; Tarakina, N. V.;

Nunes, B. N.; Adler, P.; Sahoo, S. K.; Bahnemann, D. W.; López-Salas, N. et al. Sustainable oxidation catalysis supported by light: Fe-poly (heptazine imide) as a heterogeneous single-atom photocatalyst. *Appl. Catal. B: Environ.* **2022**, *304*, 120965.

[55] Shen, S. H.; Chen, J.; Wang, Y. Q.; Dong, C. L.; Meng, F. Q.; Zhang, Q. H.; Huangfu, Y. L.; Lin, Z.; Huang, Y. C.; Li, Y. R. et al. Boosting photocatalytic hydrogen production by creating isotype heterojunctions and single-atom active sites in highly-crystallized carbon nitride. *Sci. Bull.* **2022**, *67*, 520–528.

[56] Cheng, L.; Zhang, P.; Wen, Q. Y.; Fan, J. J.; Xiang, Q. J. Copper and platinum dual-single-atoms supported on crystalline graphitic carbon nitride for enhanced photocatalytic CO_2 reduction. *Chin. J. Catal.* **2022**, *43*, 451–460.

[57] Chi, H. Y.; Chen, C. L.; Zhao, K. N.; Villalobos, L. F.; Schouwink, P. A.; Piveteau, L.; Marshall, K. P.; Liu, Q.; Han, Y.; Agrawal, K. V. Unblocking ion-occluded pore channels in poly(triazine imide) framework for proton conduction. *Angew. Chem., Int. Ed.* **2022**, *61*, e202207457.

[58] Liu, M. H.; Wei, C. G.; Zhuzhang, H.; Zhou, J. M.; Pan, Z. M.; Lin, W.; Yu, Z. Y.; Zhang, G. G.; Wang, X. C. Fully condensed poly (triazine imide) crystals: Extended π-conjugation and structural defects for overall water splitting. *Angew. Chem., Int. Ed.* **2022**, *61*, e202113389.

[59] Schwinghammer, K.; Mesch, M. B.; Duppel, V.; Ziegler, C.; Senker, J.; Lotsch, B. V. Crystalline carbon nitride nanosheets for improved visible-light hydrogen evolution. *J. Am. Chem. Soc.* **2014**, *136*, 1730–1733.

[60] Lin, L. H.; Wang, C.; Ren, W.; Ou, H. H.; Zhang, Y. F.; Wang, X. C. Photocatalytic overall water splitting by conjugated semiconductors with crystalline poly(triazine imide) frameworks. *Chem. Sci.* **2017**, *8*, 5506–5511.

[61] McGuigan, S.; Tereniak, S. J.; Donley, C. L.; Smith, A.; Jeon, S.; Zhao, F. Y.; Sampaio, R. N.; Pauly, M.; Keller, L.; Collins, L. et al. Discovery of a hybrid system for photocatalytic CO_2 reduction via attachment of a molecular cobalt-quaterpyridine complex to a crystalline carbon nitride. *ACS Appl. Energy Mater.* **2023**, *6*, 10542–10553.

[62] Nimbalkar, D. B.; Nguyen, V. C.; Shih, C. Y.; Teng, H. Melem-derived poly(heptazine imide) for effective charge transport and photocatalytic reforming of cellulose into H_2 and biochemicals under visible light. *Appl. Catal. B: Environ.* **2022**, *316*, 121601.

[63] Zeng, Z. X.; Quan, X.; Yu, H. T.; Chen, S.; Zhang, Y. B.; Zhao, H. M.; Zhang, S. S. Carbon nitride with electron storage property: Enhanced exciton dissociation for high-efficient photocatalysis. *Appl. Catal. B: Environ.* **2018**, *236*, 99–106.

[64] Kröger, J.; Jiménez-Solano, A.; Savasci, G.; Rovó, P.; Moudrakovski, I.; Küster, K.; Schlomberg, H.; Vignolo-González, H. A.; Duppel, V.; Grunenberg, L. et al. Interfacial engineering for improved photocatalysis in a charge storing 2D carbon nitride: Melamine functionalized poly(heptazine imide). *Adv. Energy Mater.* **2021**, *11*, 2003016.

[65] Liu, S. P.; Diez-Cabanes, V.; Fan, D.; Peng, L.; Fang, Y. X.; Antonietti, M.; Maurin, G. Tailoring metal-ion-doped carbon nitrides for photocatalytic oxygen evolution reaction. *ACS Catal.* **2024**, *14*, 2562–2571.

[66] Xu, Y. S.; Fan, M. J.; Yang, W. J.; Xiao, Y. H.; Zeng, L. T.; Wu, X.; Xu, Q. H.; Su, C. L.; He, Q. J. Homogeneous carbon/potassium-incorporation strategy for synthesizing red polymeric carbon nitride capable of near-infrared photocatalytic H_2 production. *Adv. Mater.* **2021**, *33*, 2101455.

[67] Savateev, A.; Pronkin, S.; Epping, J. D.; Willinger, M. G.; Wolff, C.; Neher, D.; Antonietti, M.; Dontsova, D. Potassium poly(heptazine imides) from aminotetrazoles: Shifting band gaps of carbon nitride-like materials for more efficient solar hydrogen and oxygen evolution. *ChemCatChem* **2017**, *9*, 167–174.

[68] Lu, Z.; Xu, X. T.; Wang, Z. L. Highly crystalline carbon nitride by covalent remedy for CO_2 photoreduction. *Sep. Purif. Technol.* **2024**, *330*, 125457.

[69] Xia, P. F.; Antonietti, M.; Zhu, B. C.; Heil, T.; Yu, J. G.; Cao, S. W. Designing defective crystalline carbon nitride to enable selective CO_2 photoreduction in the gas phase. *Adv. Funct. Mater.* **2019**, *29*, 1900093.

[70] Li, Y. R.; Xue, Y. Y.; Gao, X.; Wang, L. D.; Liu, X.; Wang, Z. H.; Shen, S. H. Cayanamide group functionalized crystalline carbon nitride aerogel for efficient CO_2 photoreduction. *Adv. Funct. Mater.* **2024**, *34*, 2312634.

[71] Szalad, H.; Galushchinskiy, A.; Jianu, T.; Roddatis, V.; Tarakina, N. V.; Savateev, O.; Antonietti, M.; Albero, J.; García, H. Polymeric triazine/heptazine imide heterostructures enable photocatalytic O_2 reduction to H_2O_2. *Appl. Catal. B: Environ. Energy* **2024**, *357*, 124323.

[72] Chang, J.; Zhang, T.; Qiu, S. C.; Huang, N.; Pang, D. W.; Li, H. R.; Masese, T.; Zhang, H. J.; Li, Z. Q.; Huang, Z. D. Oxygenated triazine–heptazine heterostructure creates an enormous ascension to the visible light photocatalytic hydrogen evolution performance of porous C_3N_4 nanosheets. *Small* **2023**, *19*, 2301579.

[73] Sun, Z. Z.; Dong, H. Z.; Yuan, Q.; Tan, Y. Y.; Wang, W.; Jiang, Y. B.; Wan, J. Y.; Wen, J. W.; Yang, J. J.; He, J. Q. et al. Self-supported hierarchical crystalline carbon nitride arrays with triazine–heptazine heterojunctions for highly efficient photoredox catalysis. *Chem. Eng. J.* **2022**, *435*, 134865.

[74] Zhang, J.; Liang, X. C.; Zhang, C.; Lin, L. H.; Xing, W. D.; Yu, Z. Y.; Zhang, G. G.; Wang, X. C. Improved charge separation in poly(heptazine–triazine) imides with semi-coherent interfaces for photocatalytic hydrogen evolution. *Angew. Chem., Int. Ed.* **2022**, *61*, e202210849.

[75] Sundermeyer, W. Hexamethyldisilan. *Z. Anorg. Allg. Chem.* **1961**, *310*, 50–52.

[76] Wirnhier, E.; Döblinger, M.; Gunzelmann, D.; Senker, J.; Lotsch, B. V.; Schnick, W. Poly(triazine imide) with intercalation of lithium and chloride ions $[(C_3N_3)_2(NH_xLi_{1-x})_3 \cdot LiCl]$: A crystalline 2D carbon nitride network. *Chem.—Eur. J.* **2011**, *17*, 3213–3221.

[77] Qin, J. J.; Liu, Z.; Xu, W. C.; Zhu, X. M.; Liang, F. W.; Yu, Y. T.; Zheng, Y. Z.; Yao, L.; Zhang, H. H.; Lin, K. C. et al. Heterogeneous photocatalysis coupled with Fenton-like reaction for fluoroquinolone antibiotics degradation by poly (triazine imide): From mechanism to application in a continuous flow catalytic system. *Chem. Eng. J.* **2023**, *476*, 146856.

[78] Liang, X. C.; Xue, S. K.; Yang, C.; Ye, X. Y.; Wang, Y. L.; Chen, Q. D.; Lin, W.; Hou, Y. D.; Zhang, G. G.; Shalom, M. et al. The directional crystallization process of poly (triazine imide) single crystals in molten salts. *Angew. Chem., Int. Ed.* **2023**, *62*, e202216434.

[79] Lyu, S.; Wang, J. L.; Zhou, Y. Q.; Wei, C. G.; Liang, X. C.; Yu, Z. Y.; Lin, W.; Hou, Y. D.; Yang, C. Structural lithium incorporated with the crystalline poly(triazine imide) frameworks for selective catalytic oxidative desulfurization. *Adv. Funct. Mater.* **2024**, *34*, 2310286.

[80] Yang, S. B.; Gong, Y. J.; Zhang, J. S.; Zhan, L.; Ma, L. L.; Fang, Z. Y.; Vajtai, R.; Wang, X. C.; Ajayan, P. M. Exfoliated graphitic carbon nitride nanosheets as efficient catalysts for hydrogen evolution under visible light. *Adv. Mater.* **2013**, *25*, 2452–2456.

[81] Xing, L. Z.; Yang, Q.; Zhu, C.; Bai, Y. L.; Tang, Y. R.; Rueping, M.; Cai, Y. F. Poly(heptazine imide) ligand exchange enables remarkable low catalyst loadings in heterogeneous metallaphotocatalysis. *Nat. Commun.* **2023**, *14*, 1501.

[82] Wang, J. J.; Li, P.; Wang, Y.; Liu, Z. Y.; Wang, D. Q.; Liang, J. J.; Fan, Q. H. New strategy for the persistent photocatalytic reduction of U(VI): Utilization and storage of solar energy in K^+ and cyano co-decorated poly(heptazine imide). *Adv. Sci.* **2023**, *10*, 2205542.

[83] Chueh, L. C.; Lin, T. J.; Lee, H. C.; Wu, J. J. Defective potassium poly(heptazine imide) preventing spin delocalization and hole transfer

deactivation for efficient solar energy conversion and storage. *Small* **2024**, *20*, 2304813.

[84] Ye, M. Y.; Li, S.; Zhao, X. J.; Tarakina, N. V.; Teutloff, C.; Chow, W. Y.; Bittl, R.; Thomas, A. Cobalt-exchanged poly(heptazine imides) as transition metal-N_x electrocatalysts for the oxygen evolution reaction. *Adv. Mater.* **2020**, *32*, 1903942.

[85] Podjaski, F.; Lotsch, B. V. Optoelectronics meets optoionics: Light storing carbon nitrides and beyond. *Adv. Energy Mater.* **2021**, *11*, 2003049.

[86] Lau, V. W. H.; Klose, D.; Kasap, H.; Podjaski, F.; Pignié, M. C.; Reisner, E.; Jeschke, G.; Lotsch, B. V. Dark photocatalysis: Storage of solar energy in carbon nitride for time-delayed hydrogen generation. *Angew. Chem., Int. Ed.* **2017**, *56*, 510–514.

[87] Wu, P. S.; Lin, T. J.; Hou, S. S.; Chen, C. C.; Tsai, D. L.; Huang, K. H.; Wu, J. J. Non-photochromic solar energy storage in carbon nitride surpassing blue radicals for hydrogen production. *J. Mater. Chem. A* **2022**, *10*, 7728–7738.

[88] Gouder, A.; Jiménez-Solano, A.; Vargas-Barbosa, N. M.; Podjaski, F.; Lotsch, B. V. Photomemristive sensing via charge storage in 2D carbon nitrides. *Mater. Horiz.* **2022**, *9*, 1866–1877.

[89] Ma, J.; Peng, X. X.; Zhou, Z. X.; Yang, H.; Wu, K. Q.; Fang, Z. Z.; Han, D.; Fang, Y. F.; Liu, S. Q.; Shen, Y. F. et al. Extended conjugation tuning carbon nitride for non-sacrificial H_2O_2 photosynthesis and hypoxic tumor therapy. *Angew. Chem., Int. Ed.* **2022**, *61*, e202210856.

[90] Zhang, X.; Ong'achwa Machuki, J.; Pan, W. Z.; Cai, W. B.; Xi, Z. Q.; Shen, F. Z.; Zhang, L. J.; Yang, Y.; Gao, F. L.; Guan, M. Carbon nitride hollow theranostic nanoregulators executing laser-activatable water splitting for enhanced ultrasound/fluorescence imaging and cooperative phototherapy. *ACS Nano* **2020**, *14*, 4045–4060.

[91] Ge, F. Y.; Xu, Y. G.; Zhou, Y. H.; Tian, D.; Huang, S. Q.; Xie, M.; Xu, H.; Li, H. M. Surface amorphous carbon doping of carbon nitride for efficient acceleration of electron transfer to boost photocatalytic activities. *Appl. Surf. Sci.* **2020**, *507*, 145145.

[92] Yu, Y.; Yan, W.; Wang, X. F.; Li, P.; Gao, W. Y.; Zou, H. H.; Wu, S. M.; Ding, K. J. Surface engineering for extremely enhanced charge separation and photocatalytic hydrogen evolution on g-C_3N_4. *Adv. Mater.* **2018**, *30*, 1705060.

[93] Yang, Y. L.; Zhang, D. N.; Xiang, Q. J. Plasma-modified $Ti_3C_2T_x$/CdS hybrids with oxygen-containing groups for high-efficiency photocatalytic hydrogen production. *Nanoscale* **2019**, *11*, 18797–18805.

[94] Li, Y.; Zhang, D. N.; Fan, J. J.; Xiang, Q. J. Highly crystalline carbon nitride hollow spheres with enhanced photocatalytic performance. *Chin. J. Catal.* **2021**, *42*, 627–636.

[95] Sun, Z. Z.; Tan, Y. Y.; Wan, J. Y.; Huang, L. M. In-depth understanding of the effects of intramolecular charge transfer on carbon nitride based photocatalysts. *Chin. J. Chem.* **2021**, *39*, 2044–2053.

[96] Sun, Z. Z.; Jiang, Y. B.; Zeng, L.; Huang, L. M. Intramolecular charge transfer and extended conjugate effects in donor–π–acceptor-type mesoporous carbon nitride for photocatalytic hydrogen evolution. *ChemSusChem* **2019**, *12*, 1325–1333.

[97] Niu, P.; Li, L. Photocatalytic overall water splitting of carbon nitride by band-structure modulation. *Matter* **2021**, *4*, 1765–1767.